Measuring and modeling surface energy balance closure at different temporal scales

Andrey A. Grachev • Christopher W. Fairall • Byron W. Blomquist • Harindra J. S. Fernando • Laura S. Leo • Sebastián F. Otárola-Bustos • James M. Wilczak • Katherine L. McCaffrey

Agricultural and Forest Meteorology

Manuscript

20 May 2019

Andrey A. Grachev (✉) • Byron W. Blomquist • Katherine L. McCaffrey
NOAA Earth System Research Laboratory / Cooperative Institute for Research in Environmental Sciences, University of Colorado, 325 Broadway, R/PSD3, Boulder, CO 80305-3337, USA
e-mail: Andrey.Grachev@noaa.gov

Christopher W. Fairall • James M. Wilczak
NOAA Earth System Research Laboratory, Boulder, CO, USA

Harindra J. S. Fernando • Laura S. Leo • Sebastián F. Otárola-Bustos
Department of Civil & Environmental Engineering & Earth Sciences, University of Notre Dame, Notre Dame, IN, USA

Abstract

Measurements of the surface energy fluxes (turbulent and radiative) and other ancillary atmospheric/soil parameters made in the Columbia River Basin (Oregon) in an area of complex terrain during a 10-month long portion of the second Wind Forecast Improvement Project (WFIP 2) field campaign are used to study the surface energy budget (SEB) and surface fluxes over different temporal scales. This study analyzes and discusses SEB closure based on half-hourly, daily, monthly, seasonal, and sub-annual (~10-month) temporal averages. The data were collected over all four seasons for different states of the underlying ground surface (dry, wet, and frozen). All terms of the SEB were directly measured except for the ground heat flux, which is modelled using a Priestly-Taylor type methodology using 5 levels of soil temperature and moisture. Our half-hourly direct measurements of energy balance without the estimated ground heat flux show that the sum of the turbulent sensible and latent heat fluxes systematically underestimate positive the net radiation by around 20-30% during daytime and overestimate negative net radiation at night. This imbalance of the surface energy budget is comparable to other terrestrial sites. However, on average, the residual energy imbalance is significantly reduced at daily, weekly, and monthly averaging timescales, and moreover, the SEB can be closed for this site within reasonable limits on seasonal and sub-annual timescales (311-day averaging for the entire field campaign dataset). Increasing the averaging time to daily and longer time intervals substantially reduces the ground heat flux and storage terms, because energy locally entering the soil, air column, and vegetation in the morning is released in the afternoon and evening. Averaging on daily to sub-annual timescales smooths out a hysteresis effect (phase lag) in the SEB relationship between different components. The longer averaging

times reduce random instrumental measurement errors and other uncertainties. This study shows that SEB closure is better for dry soils compared to wet soils and the statistical dependence of the turbulent fluxes and net radiation for freezing soil surfaces appears weak, if not non-existent, apparently due to lack of the latent heat of fusion term in the traditional SEB equation. A bulk flux algorithm is developed consistent with the observations.

Keywords: Bulk flux algorithm • Radiative fluxes • Surface energy budget • Time averaging • Turbulent fluxes

1 Preamble

Surface energy fluxes (turbulent, radiative, and ground heat) are important in a wide variety of applications including climate modelling, weather forecasting, land-atmosphere simulations, agricultural and forestry research, environmental impact studies, and many other applications. A direct application of the surface energy fluxes is the net surface energy budget (SEB). Energy balance closure including all components of the SEB at the air-surface interface is necessary for a better understanding of the atmosphere-surface exchange mechanisms and to improve models over representative areas and yearly timescales.

Surface energy balance closure is a formulation of the conservation of energy principle (the first law of thermodynamics). In other words, the SEB equation is a statement of how the net radiation is balanced by turbulent sensible, latent, and soil heat fluxes in the absence of other energy sources and sinks. Comprehensive SEB studies have been conducted since the 1950-60s (e.g., Lettau and Davidson 1957; Long et al. 1964). Since the late 1980s, it has become obvious that the surface energy balance cannot be closed at temporal scales less than several hours (e.g., at half-hourly and hourly averaged time scales) as reported in many studies (e.g., Wilson et al. 2002; Foken et al. 2006; Mauder et al. 2007; Cava et al. 2008; Foken 2008; Jacobs et al. 2008; Panin and Bernhofer 2008; Higgins 2012; Leuning et al. 2012; Stoy et al. 2013; Cuxart et al. 2015; Majozi et al. 2017; Gao et al. 2017 and references therein). According to field measurements, the sum of turbulent fluxes of sensible and latent heat in most cases (generally during daytime) systematically underestimates the available energy. The lack of energy balance closure at half-hourly and hourly measurements is a fundamental and pervasive problem in micrometeorology. Note, however, that in some cases the authors reported that the energy budget

can be closed within reasonable limits (e.g., Lamaud et al. 2001; Jacobs et al. 2008), but these successes are rare.

This study utilizes the data of surface fluxes (turbulent and radiative) and other ancillary atmospheric and soil data collected in the Columbia River Gorge area near Wasco, Oregon, during the 10-month long field campaign of the second Wind Forecast Improvement Project (WFIP 2) from 24 June 2016 through 1 May 2017 (year days 176–487 with respect to 1 January 2016). The WFIP 2 project is a four-year multi-disciplinary effort intended to improve short-term weather forecast models and better understand various unresolved physical processes that affect wind energy generation in regions of complex terrain such as coastlines, mountains, and canyons, in order to develop and evaluate improved surface-flux parameterizations. The observational phase of the WFIP 2 allows an analysis of SEB for different soils over a broad range of temporal scales based on first principles.

The main objectives of this study are twofold. The first objective is an investigation of the non-closure of the SEB for three different type of soils (dry, wet, and frozen surfaces) using the same instruments, experimental setup, location, and data processing. The second objective is an analysis of SEB closure at different temporal scales from half-hourly to daily and even monthly, seasonal and sub-annual averaged time series. In some sense, this study bridges micrometeorological measurements and climatological timescales through temporal averaging. The layout of the paper is as follows. The theoretical background (basic SEB equations) and the energy balance closure problem are considered in Section 2. Instruments, data collection and site descriptions are documented in Section 3. Main findings of the study based on analysis of the WFIP 2 experimental data (e.g., time series, SEB at different timescales, and over different types of soil surfaces) are described in Section 4. Using uninterrupted time series ("golden files") for

dry and wet soils described in Sub-section 4.4, we develop and verify a bulk turbulent flux algorithm for computing surface fluxes from readily measured or modelled bulk quantities (Section 5). The conclusions are summarized in Section 6.

2 The Surface Energy Balance Closure Problem

The law of conservation of energy at the interface between atmosphere and land in the absence of other energy sources and sinks is written as:

$$H_S + H_L + G = R_{net} \tag{1}$$

where G is the soil heat flux, R_{net} is the net radiation defined as the balance between downwelling (incoming) and upwelling (outgoing) SW and LW radiation:

$$R_{net} = SW_{down} - SW_{up} + LW_{down} - LW_{up} \tag{2}$$

The turbulent fluxes of sensible heat H_S and latent heat H_L in (1) can be estimated by the eddy correlation method according to

$$H_S = c_p \rho \overline{w'\theta'} \tag{3}$$

$$H_L = \mathcal{L}_e \rho \overline{w'q'} \tag{4}$$

where ρ is the mean air density, θ is the air potential temperature, q is the air specific humidity, c_p is the specific heat capacity of air at constant pressure, and $\mathcal{L}_e$ is the latent heat of evaporation of water. Here w is the vertical velocity component, the prime [$'$] denotes fluctuations about the mean value, and an overbar is an averaging operator (half an hour in this study).

As mentioned above, numerous direct measurements of all SEB components in (1) have shown that over land the sum $H_S + H_L + G$ in most cases (generally during daytime) systematically underestimate the net radiation R_{net} by about 20-30% (Foken and Oncley 1995;

Wilson et al. 2002; Meyers and Hollinger 2004; Foken et al. 2006; Mauder et al. 2007; Cava et al. 2008; Foken 2008; Jacobs et al. 2008; Panin and Bernhofer 2008; Higgins 2012; Leuning et al. 2012; Stoy et al. 2013; Masseroni et al. 2014; Gao et al. 2017).

Because the energy balance at the surface often cannot be closed based on experimental observations, the SEB equation (1) is typically formulated as (e.g., Foken et al. 2006):

$$H_S + H_L + G + Res = R_{net} \tag{5}$$

where Res is any residual term (imbalance). Equation (1) assumes an ideal case, when all the fluxes are measured at the infinitesimal interface between an atmosphere and a soil, while Eq. (5) implies a two-layer (atmosphere and soil) column of finite thickness (e.g., Foken 2006, his Fig. 1). The turbulent and soil fluxes in (5) are measured at the upper and lower boundary planes of the total layer respectively. Clearly a variety of factors may be responsible for the lack of SEB closure in the layer (e.g., Foken et al. 2006; Mauder et al. 2007; Higgins 2012; Leuning et al. 2012). Therefore, in general Res can be partitioned as:

$$Res = T + S + X \tag{6}$$

where T is an additional transport (vertical and horizontal) through all boundary planes, S is a total storage in the two-layer column, and X indicates all other unspecified contributions to (1).

The additional transport term T in (6) includes the divergence of the horizontal turbulent flux caused by complex terrain or heterogeneities in the underlying surface and soil heat transfer by convection or circulation (in addition to conductive heat flux G) and/or by convective water flux in the water-saturated soils at the bottom plane (the water flux in the soil is a consequence of the law of conservation of mass in the case $H_L \neq 0$). The storage term, S, can be partitioned as (e.g., Meyers and Hollinger 2004, Leuning et al. 2012, Masseroni et al. 2014):

$$S = S_a + S_g + S_p + S_c + S_x \tag{7}$$

Where S_a is storage of energy in the air column due to radiative and/or sensible heat flux divergence (the air enthalpy change), S_g is the ground heat storage above the soil heat plate measurement level, S_p is the radiation consumed in photosynthesis (the photosynthesis flux), S_c is the canopy heat storage in biomass (the rate change in enthalpy of the vegetation), and S_x is all other storage terms, e.g. the atmospheric moisture change and the canopy dew water enthalpy change (Jacobs et al. 2008). The term X in Eq. (6) may include several factors: loss of low-frequency covariance contributions to the turbulent fluxes induced by insufficient averaging time and/or inadequate resolution of high-frequency flux components; choice of coordinate systems; the mismatch between the footprint of the turbulent heat fluxes and the measurements of radiation components and soil heat fluxes; instrumental errors; the latent heat of fusion term (see below); etc. The lack of SEB closure raises concerns regarding eddy covariance measurements at standard half-hourly and hourly averaging time scales. There are suggestions that increasing averaging time can improve SEB closure by capturing additional sensible and latent heat fluxes at low-frequencies (e.g., Foken 2008).

Recall that failure to close the energy balance is associated with a systematic bias. In particular for the positive net radiation, $R_{net} > 0$ (generally during daytime), the left-hand side of Eq. (1) is routinely smaller than the right-hand side ($Res > 0$ in Eq. 5). An immediate problem for the additional terms (6) is that the different terms contribute differently (either positively or negatively) to the bias. While all the storage terms (7) and the loss of high-frequency components in the turbulent fluxes contribute positively to *Res* in the case $R_{net} > 0$, it is difficult to see why the loss of low-frequency covariance associated with local circulations would always lead to an underestimation of the turbulent fluxes, and the same could be said about advection (Finnigan 2008). For example, according to SHEBA data (Grachev et al. 2005, Fig. 8), the low-

frequency flux components can be both positive and negative. Thus, while the storage term S in Eq. (6) is always positive (systematic contribution) for the positive net radiation, the other two terms, T and X, contribute positively or negatively to the bias (random contribution).

The various terms in Eq. (1) differ greatly in magnitude. Generally the soil heat flux G is relatively small as compared with the net radiation, but in some cases the G term in Eq. (1) cannot be ignored. For example, midday values of the ratio of the soil heat flux and the net radiation, G/R_{net}, are about 0.15 for measurements over fields of bare soil, alfalfa, and cotton near Phoenix, AZ according to Kustas and Daughtry (1990), and 0.14-0.17 for a no-till cornfield in central Iowa in November (Sauer et al. 1998). However, the ratio G/R_{net} can generally vary between 0.05 and 0.50, depending on the period of the day, thermal properties of the soil, surface cover, soil moisture content, and solar irradiance (Kustas et al. 1993). In particular, during the night or in the fall/winter, G is an important term in (1), when R_{net} is low and stable atmospheric conditions cause H_S and H_L to be small. Despite relative importance, the soil heat flux is not often measured, including this study where the observational site was not instrumented with a heat flux plate.

The soil heat flux can be estimated from soil temperature profile measurements using Fourier's Law of Heat Conduction (gradient method)

$$G(z) = -\lambda \frac{\partial T_S}{\partial z} \tag{8}$$

where λ is the thermal conductivity of the soil and $\partial T_S/\partial z$ is the vertical temperature gradient of the soil temperature, T_S. In practical applications the first derivative of the soil temperature in (8) is usually replaced by the finite-difference approximation in the soil layer Δz and Eq. (8) reduces to $G(z) \approx -\lambda \Delta T_S/\Delta z$. Fourier's Law (8) presumes steady state heat conduction, one-dimensional heat flow, an isotropic and homogeneous material, constant thermal conductivity λ, and no

internal heat generation. Generally, soil is a three-phase material (water, air, solid) and application of Eq. (8) is considerably more difficult. The thermal conductivity of soil depends on the conductivity of each phase and their proportions; that is, λ varies by composition of the solid fraction (e.g., mineral type and particle size), water content (thermal conductivity of water is about two to three times greater than that of soil), amount of organic matter, and bulk density. As a result, λ values can change between layers within Δz even for the same soil due to changes in water content. Another complexity of the gradient method (8) is associated with non-stationarity (diurnal variations), even during a half-hour averaging period. The diurnal cycle of solar radiation modulates a sinusoidal variation in the ground surface heat flux and diurnal thermal waves in the top soil layer. The temperature wave damps exponentially with depth and its lag time increases with depth. The ground heat flux is theoretically $\pi/4$ (1/8 cycle) out of phase with the temperature wave (hysteresis effect); that is, the ground heat flux is largest three hours ahead of the surface temperature for a diurnally varying surface temperature cycle (Arya 1988; Garratt 1992; Gao et al. 2010). Thus, while the gradient method (8) is simple to employ under field conditions, accurate measurement of λ and the vertical soil temperature gradient is challenging. The impact of the hysteresis effect in diurnal cycles and the effect of the wave phase difference between different atmospheric and/or soil variables on the SEB closure are discussed in number of studies (e.g., Gao et al. 2010, 2017; Sun et al. 2013).

Direct measurements of the turbulent flux of carbon dioxide allow estimation of a storage term S_p in (7) associated with the photosynthesis flux. The photosynthesis flux S_p is the change in the Gibbs free energy and, according to Nobel (2009, Chapter 6.5, p. 313), about 479 kJ of energy is stored per mole of CO_2 fixed into photosynthetic products; that is, S_p [W m^{-2}] = −0.479 F_{CO_2} [μmol m^{-2} s^{-1}]. For example, a canopy assimilation rate of F_{CO_2} =10 μmol m^{-2} s^{-1} equates to

energy flux of $S_p = 4.79 \approx 5$ W m^{-2} (cf., Meyers and Hollinger 2004, their Fig. 5 and Masseroni et al. 2014, their Fig. 3). Thus, the photosynthesis storage term is relatively small; according to estimate by Finnigan (2008), $S_p \approx 0.01 R_{net}$. The canopy heat storage term (e.g., because of changes in leaf temperature), S_c, may be also a factor in the lack of closure, but it cannot be easily assessed and flux values cannot be easily corrected for this influence in the framework of our study. According to Meyers and Hollinger (2004, Figs. 4 and 5) and Masseroni et al. (2014, Fig. 3), generally $S_c \leq S_p$. Although the soil heat flux G in Eq. (5) and the storage terms S_a and S_g in Eq. (7) can be estimated from the observations, their contribution to SEB closure at half-hourly time scales lies beyond the scope of this study.

The SEB (1) and the fact that the turbulent fluxes are highly correlated with the net radiation (e.g., see results presented in Section 4 shortly) provide an objective approach to estimate turbulent fluxes independently of a conventional bulk flux algorithm. Traditionally, the SEB is considered closed in numerical models of the climate system and in other applications (e.g., for remote sensing), allowing for estimation of missing terms as the residual of the others (e.g., Cuxart et al. 2015 and references therein). Similar ideas are used in soil-vegetation-atmosphere transfer schemes where H_S and H_L are estimated from thermal infra-red data (i.e. radiometric surface temperature) and SEB, Eq. (1) (e.g., Priestley and Taylor 1972; Su 2002; Kustas et al. 2004; Ezzahar et al. 2012; Yao et al. 2015 and references therein).

3 Observation Site and Instrumentation

Figure 1 shows the study area located along the Columbia River Gorge in eastern Oregon and Washington states. This region was chosen because of its combination of complex terrain

and extensive wind farm development. These measurements provide insight into the structure and evolution of atmospheric flows and other physical processes in complex terrain leading to improvements in parametrization of subgrid-scale processes in NWP models to support wind energy forecasting. Federal agencies, private companies, and universities collaborated on the WFIP 2 project, deploying wind profiling radars, sodars, lidars, networks of tall meteorological towers, and other instruments across a range of spatial scales (Figs. 1 and 2).

In this observational study we use measurements of half-hourly averaged turbulent and radiative fluxes, surface meteorology, and basic soil parameters from the Physics Site 1 tower (PS01, 45.64°N and 120.68°W) located near Wasco, Oregon, (Fig. 1) to examine SEB closure over different soil conditions (dry, wet, and frozen) and at different averaging timescales. Turbulent fluxes and mean meteorological data were measured continuously on a 10-m meteorological tower at two levels, nominally 3 m and 10 m (Fig. 2). Each level was instrumented with identical fast response three-axis sonic anemometers sampling wind velocity and sonic temperature at 20 Hz (R.M. Young Model 81000) and Rotronics HC2S3 temperature and relative humidity probes (T/RH , sampling frequency = 1 Hz). The HC2S3 probes were housed in ventilated radiation shields. A fast-response (20 Hz) open path infrared gas analyzer (LI-7500, LI-COR Inc.) was collocated at 3-m height with the lower sonic anemometer for direct measurements of water vapor turbulent flux and other relevant turbulent statistics. Measurements were collected by a data-logger (Campbell CR3000) and successively parsed into 15-minute data files for cell-modem network transmission to remote data storage.

Tower-based eddy covariance measurements provide a long-term near continuous temporal record of half-hourly averaged turbulent mass and energy fluxes. The mean wind speed and wind direction were derived from the sonic anemometers, with rotation of the measurement

axes to place the measured wind components in a streamline coordinate system based on half-hour averaged 20-Hz data. In this study, we performed tilt-corrections of the sonic anemometer data using the "planar-fit" method rotation of the coordinate system proposed by Wilczak et al. (2001), which essentially fits a climatological plane through the streamlines of the local flow. The planar-fit angles were calculated from 30-min averages at each level over the 10-month dataset (for the period 24 June 2016 to 01 May 2017). Several data-quality indicators based on objective and subjective methods have been applied to the original flux data to remove spurious or low-quality records. Specifically, turbulent data have been edited for unfavorable relative wind direction for which the tower was upwind of the sonic anemometers, non-stationarity, minimum or/and maximum thresholds for the turbulent statistics, etc. Based on established criteria, the best flux estimates have been used (e.g., Bariteau et al. 2010; Grachev et al. 2011; Blomquist et al. 2014 and references therein).

Measurements of soil temperature and moisture were made at five levels located nominally at 5, 10, 20, 50, and 100 cm depths below the ground surface approximately 5 m from the flux tower. Campbell Scientific 107 temperature sensors and a CS616 water content reflectometer were used to measure temperature and soil moisture (in volumetric water content) respectively. No direct measurements of surface soil heat flux with a heat flux plate were performed at this site. The soils at the WFIP 2 Physics Site PS01 are primarily well-drained silt (73%), with minor components of sand (14%), and clay (13%) and average 152 cm in depth before reaching harder rock (water table).

The downwelling and upwelling radiation was measured from two radiation masts located near the flux tower (Fig. 2). Eppley pyranometer (PSP) and pyrgeometer (PIR) are used to measure the shortwave and infrared radiation. Both 'slow'-response radiation and soil data

reported here are based on raw measurements sampled at 1 Hz which were subsequently averaged over 1-min time intervals and recorded by a data-logger. The instrument suite located on the tower was operated by University of Notre Dame scientists; solar radiation and soil science instruments were conducted by the NOAA/ESRL team.

4 Analysis of the WFIP 2 Data

4.1 Time Series

In this sub-section, we analyze the time series of half-hour averaged surface fluxes and basic meteorological variables to describe weather and soil conditions, surface fluxes, and other relevant variables as observed during the entire WFIP 2 field campaign for the period 24 June 2016 to 01 May 2017 (Year Days 176-487 with respect to January 1, 2016 UTC). Figures 3 and 4 show the time series of 'slow' half-hourly averaged basic meteorological variables collected at the Physics Site PS01 near Wasco, Oregon (Fig. 2), except for the rain rate which was measured near another observational site located near the Wasco State Airport (WCO). Figure 5 shows the time series of short-wave (SW) and long-wave (LW) radiation (downwelling and upwelling), radiation budgets, and also the surface albedo observed at Physics Site PS01. By convention, radiation fluxes are positive when directed toward the surface, fluxes away are negative. The net radiation describes the balance between incoming (downwelling) and outgoing (upwelling) SW and LW radiation. The surface albedo in Fig. 5d is derived from the ratio of the upwelling SW radiation to the downwelling SW radiation. Time series of friction velocity $u_* = \sqrt{-\overline{w'u'}}$, sensible H_S and latent H_L heat fluxes defined by Eqs. (3)–(4) are shown in Fig. 6.

The air and soil temperatures display the familiar strong seasonal trend with maximum in mid-summer and minimum during winter (Figs. 3c and 4a). The onset of near-surface soil freezing occurred in the autumn on about days 343–344 (8–9 December 2016). Frozen ground started warming when the gradient of the subsurface temperature changed sign on about days 428–429 (3–4 March 2017). The air temperatures rise above freezing during spring melt on about days 424–425 (27–28 February 2017). The rather constant temperature of the soil at 5 and 10-cm levels near 0°C (Fig. 4a) on about days 344–428 (9 December 2016–3 March 2017) is due to the snow cover when present (cf. Fig. 5d), to the rather high moisture content of the soil (Fig. 4b), and to releasing latent heat of fusion of soil water as soil freezes. The near-zero topsoil temperatures on these days are due to the phase transition of water to ice and are associated with the so-called "zero-curtain" effect (e.g., Grachev et al. 2018 and reference therein). Release of latent heat during the freezing of pore water results in the maintenance of isothermal temperatures at or around 0°C within the freezing ground layer over extended periods (Fig. 4a).

The date of the first snowfall and the occurrence of the snow-free date are determined radiometrically as the date when the surface albedo first rises above and drops below 30% respectively (Stone et al. 2002). According to Fig. 5d, the albedo increases suddenly on days 342–344 (7–9 December 2016) with the first snowfall. The date of snow melt is evidenced by the large reduction in albedo that occurs on days 425–426 (28 February–1 March 2017), i.e., when the snow cover essentially disappears (Fig. 5d).

The annual cycle of the downwelling SW radiation SW_{down} is clearly evident with maximum flux values in mid-summer of about 940 to 960 W/m^2 (Fig. 5a) and values that drop to minimum during winter months. Similarly, the downwelling longwave radiation LW_{down} reaches a minimum in winter and a maximum in summer (Fig. 5b). The net radiation R_{net} is weakly

negative during winter months (Fig. 5c). The peak in R_{net} occurs during spring/summer when the snow melts and SW_{down} is near the annual peak (Fig. 5).

Figure 6 shows the seasonal cycles of the friction velocity and the turbulent fluxes of the sensible heat, and latent heat. The annual course of the sensible heat flux and the net radiation, R_{net} are qualitatively very similar (cf. Figs. 5c and 6b) because the balance between solar and longwave radiation is the principal energy source for daytime surface warming and evaporation (see Eq. 1). Concurrently, the annual course of the latent heat flux shown in Fig. 6c depends on both R_{net} according to Eq. 1 and soil moisture (Fig. 4a). Figure 6 shows that during the winter and cold seasons, the sensible and latent heat fluxes were small and mostly irregular when the ground is covered with snow and air temperatures are generally below freezing. However, the turbulent fluxes increase rapidly in magnitude when air temperatures rise above freezing during spring melt and eventually reach a summer maximum (cf. Figs. 3 and 6).

Based on the seasonal behaviour of the surface fluxes and surface meteorology shown in Figs. 3-6 for the entire field campaign (from 24 June 2016 to 01 May 2017), we sort the data into three categories separated by threshold values deduced from the time series of soil temperature (Fig. 4a) and soil moisture at 5 cm depth (Fig. 4b). We distinguish three soil conditions:

(i) Dry bare or lightly vegetated soil surfaces, the soil temperature at 5 cm depth > 1°C and the soil moisture at 5 cm depth ≤ 0.07;

(ii) Wet bare or lightly vegetated soil surfaces, the soil temperature at 5 cm depth > 1°C and the soil moisture at 5 cm depth > 0.07;

(iii) Frozen (snow covered) soils surfaces, the soil temperature at 5 cm depth ≤ 1°C.

Soil moisture content above is measured as the ratio of the volume of liquid water to soil volume.

4.2 SEB at different timescales

The closure of the SEB (1) during the entire field campaign is shown in Fig. 7. Fig. 7a shows a scatter plot of the sum of the sensible and latent heat fluxes versus the net solar radiation for half-hourly averaged fluxes. Fig. 7b presents a similar plot based on daily, monthly, and sub-annual (311 days) averages. Note that the daily, weekly, monthly etc. data points in this study are derived from the original half-hourly averaged fluxes averaged over longer time scales. Recall also that the soil heat flux, G, is not used for the SEB closure analysis (e.g., in Fig. 7) since measurements of G were not available. Our direct measurements of SEB in Fig. 7a are roughly consistent with past eddy-covariance results over land showing that the sum of H_S and H_L systematically underestimate the net radiation for $R_{net} > 0$ (generally during daytime convective conditions) and overestimate for $R_{net} < 0$ (generally during nocturnal boundary layer). According to Fig. 7a, the linear regression forced through the origin for the half-hourly data is $y = 0.77x$ with the correlation coefficient $R^2 = 0.94$ (number of data points, $N = 3624$) in the case $R_{net} > 0$ (dashed magenta line) and the regression is $y = 0.27x$ with $R^2 = 0.41$ and $N = 897$ in the case $R_{net} < 0$ (dotted red line). In total for both positive and negative R_{net} the linear regression forced through the origin is $y = 0.76x$ (not shown) with $R^2 = 0.95$ and $N = 4521$.

Thus, the SEB imbalance for half-hourly averaged fluxes over the entire WFIP 2 field campaign (from 24 June 2016 to 01 May 2017) is about 24%. This mean imbalance is generally consistent with other efforts to close the SEB (e.g., Foken and Oncley 1995; Wilson et al., 2002; Meyers and Hollinger 2004; Foken et al., 2006; Cava et al. 2008; Foken 2008; Jacobs et al. 2008; Panin and Bernhofer 2008; Higgins 2012; Leuning et al., 2012; Stoy et al., 2013; Masseroni et al., 2014; Cuxart et al., 2015; Gao et al., 2017). Despite multiple review papers that discuss the

lack of energy closure at half-hourly and hourly averaged timescales, and the myriad of studies devoted to the investigation of the individual factors of the imbalance at these averaging period, the SEB closure at the longer averaging times (from the daily to sub-annual timescales) has not been systematically examined. Previous work by Leuning et al. (2012) has shown that energy closure is observed at only 8% of flux sites in the La Thuile synthesis dataset (produced after a workshop in La Thuile, Italy, in February, 2007) with half-hourly averages but this increases up to 45% of sites using daily averages. Recent work by Reed et al. (2018) examined the effect of temporal variation in the SEB in annual and sub-annual timescales for different site locations.

In general, increasing the averaging time consistently from half-hourly to daily and longer time intervals substantially reduces the SEB imbalance. According to Fig. 7b, the linear regression forced through the origin is $y = 0.87x$ with the correlation coefficient $R^2 = 0.78$ ($N = 243$) in the case of daily averages (green circles and dashed magenta line) and in the case monthly (30-day) averages the regression is $y = 0.91x$ with $R^2 = 0.99$ and $N = 10$ (i.e., ten full months, blue triangles and dotted red line). Moreover, the SEB can be closed for this site within several percent on sub-annual timescale (red star); that is, $< H_S > + < H_L > = 1.02 < R_{net} >$ where $< \cdots >$ denotes here an averaging operator (the arithmetic mean) for all available half-hourly values of the surface energy fluxes during the entire field campaign (311-day dataset).

On average, the scatter plots of the daily and monthly averaged data (Fig. 7b) show substantial reduction of the SEB imbalance. However, the SEB imbalance may be worse at daily timescales (cf., Leuning et al., 2012), and in a select number of cases still occur in the monthly averages (cf., Reed et al., 2018), implying some processes extend beyond daily and monthly timescales. In the next sub-section, we consider some of the factors leading to these biases.

4.3 SEB over different types of soil surfaces

In this sub-section, we consider the SEB over the entire field campaign at different time scales for the three soil conditions identified in Section 4.1. Figure 8 shows scatter plot of the turbulent flux terms in Eq. (1) versus R_{net} at half-hourly resolution observed from 24 June 2016 to 01 May 2017 for three different soil surfaces (dry, wet, and frozen). The turbulent fluxes of the sensible and latent heat shown in Fig. 8a, b increase systematically with increasing the net radiation because R_{net} is normally the principal source of energy for daytime warming of the surface and evaporation. We note different slopes of the bin-averaged fluxes for different soil conditions. According to Fig. 8a, the bin-averaged dependence of H_S is generally steeper for drier than for wetter soils, whereas situation with H_L is obviously opposite; the latent heat flux is small over dry soil surfaces indicating that evaporation is negligible (Fig. 8b). Note also that sensible and latent heat fluxes are comparable over wet soil surfaces and Bowen ratio $Bo = H_S/H_L$ averaged around 1 during daytime (not shown). It can be assumed that wet and/or water-saturated soils, which have larger heat storage due to high specific heat capacity and higher thermal conductivity, cause the observed behaviour of H_S and H_L versus R_{net} in Fig. 8.

According to bin-averaged data Fig. 8c, closure is lower for wet soils compared to dry soils. The statistical dependence of the turbulent fluxes and R_{net} for frozen soil surfaces appears weak, if not non-existent (Fig. 8c). As mentioned in Section 4.1, during the cold season topsoil temperatures remain close to 0°C and the soil heat flux term in Eq. (1) G = 0 for a while. This isothermal freezing process is referred to as the "zero-curtain" effect (e.g., Grachev et al. 2018). Under such conditions, the latent heat of fusion term must be added to Eq. (1). The nature of this term is associated with the change between the liquid and solid phases, as when water turns to

ice. The absence of the latent heat of fusion term in the SEB equation explains why the Eq. (1) doesn't work for the case of frozen soil surfaces as shown in Fig. 8c. However, a detailed discussion of the SEB during the zero-curtain period is beyond the scope of this paper.

The linear regression forced through the origin (not shown) for the dry soil data shown in Fig. 8c is $y = 0.80x$ with the correlation coefficient, $R^2 = 0.97$ ($N = 1993$); that is, SEB imbalance is 20% in this case. For wet soils over the entire field campaign (Fig. 8c), the linear regression forced through the origin is $y = 0.73x$, $R^2 = 0.92$ ($N = 1739$), implying that there is an imbalance of 27%, which is high but not unusual. The linear regression of Fig. 8c for the frozen (snow covered) soil surfaces is $y = 0.079x$, $R^2 = 0.22$ ($N = 683$), implying a weak correlation between the turbulent fluxes and the net radiation. Thus, the SEB in the form of Eq. (1) cannot be applied to freezing soil surfaces without the inclusion of a latent heat of fusion term.

Our results for the SEB closure over dry and wet soils are consistent with prior studies. According to Roxy et al. (2014), SEB closures were lower when the latent heat fluxes were highest, mainly during wet periods; the mean SEB closure was found to be 0.742 and 0.795 for wet and dry seasons, respectively. Cuxart et al. (2015) reported that very large imbalances are related to high values of soil moisture, especially in warm conditions. However, a multi-year analysis by Majozi et al. (2017) revealed SEB closure 0.93±0.11 with the dry season having the imbalance 0.70 while the mean SEB closure during the wet season was 1.12.

Figure 9 shows that increasing the averaging time from half-hourly to daily and longer time intervals substantially reduces the SEB imbalance for each soil type (though with some reservations for the frozen soils). For dry soils in Fig. 9a, the linear regression for daily averages forced through the origin is $y = 0.92x$ with the correlation coefficient $R^2 = 0.98$ ($N = 81$) and the SEB can be closed within one percent on a seasonal timescale (red six-pointed star). For wet

soils (Fig. 9b), the linear regression of daily averages is $y = 0.79x$, $R^2 = 0.92$ ($N = 92$) and the SEB closure is 0.95 at a seasonal timescale. For frozen soil surfaces (Fig. 9c), the SEB closure is 0.06, R^2 =0.02 at daily timescales and 0.34 at a seasonal timescale.

Although, increasing the averaging time from half-hourly (Fig. 8c) to daily and longer time intervals (Fig. 9) consistently reduces the SEB imbalance for each specific soil condition, the situation is not so obvious if we compare the SEB imbalance between different soil types. For example, the SEB closure at half-hourly resolution for dry soils (0.80) may be approximately the same as the SEB closure for wet soils (0.79) at longer (monthly) timescales. In addition, the SEB imbalance may be worse at monthly timescales for wet (0.89) and frozen (0.13) soils compared to daily averages (0.92) for dry soils. Thus, our results support and clarify previous findings by Leuning et al. (2012) and Reed et al. (2018) where in a select number of cases, increasing the averaging time does not always lead to reduction of the SEB imbalance because SEB closures were compared for different sites or different seasons.

4.4 Case studies: the uninterrupted time series ("golden files")

In the previous sections, we considered the SEB imbalance based on measurements over the entire WFIP 2 field campaign (311-day dataset from 24 June 2016 to 01 May 2017) with and without separation into the different soil conditions. However, in situ data often contain gaps, from very short (few hours) up to relatively long (few weeks, Figs. 3-7). Occasional gaps in the data time series are mainly due to equipment failures, calibrations and maintenance operations or general system breakdown. Data quality assurance/control procedures lead to the rejection of "bad" data, generating additional gaps in the data records. Averaging of the fragmented data sets

raises issues in the interpretation of the results. Gap-filling techniques (e.g., interpolation for short gaps) are commonly used to estimate the missing data. However, this procedure replaces missing empirical data by simulated synthetic values that can introduce more errors.

To overcome these limitations, we consider the longest available uninterrupted time series of relatively good data for each soil condition defined in Section 4.1 ("golden files"). Figures 10-12 show continuous monthly (30-day long) records of the SEB components for dry, wet, and frozen soils respectively. From data in Figs. 10-12, the mean SEB closure (the slope of a linear regression line with forced origin) for half-hourly averaged data is 0.80 for the dry soils ($N = 1405$), 0.73 for wet soils ($N = 1201$), and 0.12 for frozen soils ($N = 988$). Note that the number of the half-hourly averaged data points in the case of dry (Fig. 10), wet (Fig. 11), and frozen (Fig. 12) soils is less of the maximum amount possible for one month ($N = 1440 = 48 \times 30$) due to quality control. For daily averages the mean SEB closure is 1.02, 0.82, and 0.22 for dry (Fig. 10), wet (Fig. 11), and frozen (Fig. 12) soils respectively ($N = 30$ for each soil type). Thus, the SEB can be closed for the dry soil within about two percent on a daily timescale for "golden files" data in Fig. 10. Further, the mean SEB closure based on the one-month averages for the data in Figs. 10-12 are 1.06 (dry soil), 0.86 (wet soil), and 0.19 (frozen soil). Thus, the results based on the almost uninterrupted 30-day time series of fluxes ("golden files", Figs. 10-12) support our previous findings derived from the data collected during the entire 311-day field campaign (gapped time series). That is: (i) increasing the averaging time from half-hourly to daily and monthly intervals generally reduces the SEB imbalance for specific type of soil; and (ii) the SEB closure is lower for the wet soils compared to dry soils (e.g., 0.73 vs. 0.80 respectively at half-hourly resolution), while closure is only ≈ 12% for frozen soils, apparently

due to the lack of a latent heat of fusion term in (1). One can estimate the missing latent heat of fusion term in (1) should be ≈ 0.8-0.9 of R_{net} to close the SEB during the cold season.

As expected, the SEB flux components and the topsoil temperature difference series have a pronounced diurnal cycle (generally for dry and wet soils). On the diurnal time scale, variations in the turbulent heat fluxes are dominantly forced by daily rhythms in the incoming solar radiation, which also drives changes in the air and soil temperatures. Furthermore, diurnal variations of the residual energy are also observed for both dry (Fig. 10c) and wet (Fig. 11c) soils. According to Figs. 10c and 11c, the daily patterns of the residual energy are characterised by positive values during the first part of the day and by a sign reversal in the second half of the day. Thus, the observed daily patterns of the residual energy (Figs. 10c and 11c) confirm that the SEB is more easily balanced at daily averaging timescales than half-hourly because of the cancellation of energy residuals of opposite sign. The diurnal variations of the residual energy reported here (Figs. 10c and 11c) are generally in good agreement with previously published results (e.g., Lamaud et al. 2001; Cava et al. 2008; Higgins 2012). The difference of the soil temperature between 10 cm and 5 cm levels for dry, wet, and frozen soils is shown in Figs. 10d, 11d, and 12d respectively. This temperature difference is ultimately related to the ground heat flux G through Eq. (8). In general, the diurnal cycle of solar radiation modulates a sinusoidal variation of the temperature difference in top soil layer (Figs. 10d and 11d) and, therefore, the ground surface heat flux and diurnal temperature waves. Thereby, much of the energy that enters the soil during the day returns to the atmosphere at night through terrestrial longwave radiation.

Figure 13 summarizes the SEB closure at different temporal scales. The red symbols and lines in Fig. 13 represent all measurements. The SEB imbalance categorized by soil condition are shown in Fig. 13 as green symbols and lines (dry soils), blue symbols and lines (wet soils), and

cyan symbols and lines (frozen soils), respectively. Figure 13 is the visual representation of our primary findings; that is, increasing the averaging time from half-hourly to longer time intervals substantially reduces the SEB imbalance and the closure is lower for the wet soils as compared to dry soils whereas the SEB closure for frozen soils is very poor, if not non-existent.

5 Bulk Parameterization of the Heat Fluxes

Atmospheric models or SEB studies almost always estimate the turbulent fluxes of momentum τ, sensible heat H_S, Eq. (3), and latent heat H_L from a bulk flux algorithm. Here, we describe the formulation developed for terrestrial situations, which is in part based on the COARE bulk flux algorithm derived for open ocean (Fairall et al. 1996, 2003), and the SHEBA bulk flux algorithm developed for sea ice conditions (Andreas et al. 2010a, 2010b). We will use observations from the WFIP 2 Physics Site PS01 to evaluate bulk representations of turbulent and ground fluxes, including the turbulent surface stress, τ, because it is required for surface layer similarity theory that forms the basis of bulk turbulent flux algorithms.

The turbulent fluxes are parameterized by bulk aerodynamic relationships, which relate fluxes to mean properties of the flow through the height-dependent transfer coefficients: C_D (the drag coefficient), C_H (the Stanton number), and C_E (the Dalton number):

$$\tau = \rho\overline{w'u'} = C_D\rho SU \tag{9}$$

$$H_S = C_H c_p \rho S(\theta_0 - \theta_a) \tag{10}$$

$$H_L = C_E \mathcal{L}_e \rho S(q_0 - q_a) \tag{11}$$

where subscripts 'zero' and a for the potential temperature θ and the air specific humidity q denote their surface and atmospheric reference height values respectively. It is often assumed

that the water vapour and other scalars (e.g. carbon dioxide and methane) are transported similarly to the temperature, i.e. with the same efficiency (the Lewis analogy) and, therefore, $C_H = C_E$. Note, that accurate estimation of the transfer coefficients in (9)-(11) is a crucial problem of air-sea/land interaction. The transfer coefficients depend on stratification (atmospheric stability) and roughness lengths (e.g., Fairall et al. 2003).

In Eq. (9) – (11), we make a distinction between the scalar averaged wind speed (i.e., the mean wind speed), S, and the vector averaged wind speed (i.e., the magnitude of the mean wind vector), U, at reference height z (see Grachev et al. 1998, Section 3.1 for discussion). The vector averaging of the wind speed first takes average and of the longitudinal and lateral wind speed components, u and v respectively, then take the square,

$$U = \left(\overline{u}^2 + \overline{v}^2\right)^{1/2} \tag{12}$$

whereas the scalar averaging firstly takes the square and then average,

$$S = \left(\overline{u^2} + \overline{v^2}\right)^{1/2} \tag{13}$$

Combining (12) and (13) with the definition of variance leads to a relationship between U and S:

$$S^2 - U^2 = \left(\overline{u^2} - \overline{u}^2\right) + \left(\overline{v^2} - \overline{v}^2\right) = \sigma_u^2 + \sigma_v^2 \tag{14}$$

where σ_u and σ_v are the horizontal velocity variances. Relationship (14) is also known as the gustiness assumption (e.g., Fairall et al. 1996; Grachev et al. 1998). In convective conditions, large-scale circulations embracing the entire convective boundary layer (CBL) create random gusts that crucially affect the surface fluxes. According to (14), S in such conditions is the vector sum U and the convective gustiness velocity, $U_G = (\sigma_u^2 + \sigma_v^2)^{1/2}$:

$$S^2 = U^2 + U_G^2 \tag{15}$$

In the COARE bulk algorithm, $U_G = \beta w_*$ where $\beta \approx 1.25$ (Fairall et al. 1996) and $w_* = \left(\overline{w'\theta_v'} g h/\theta_v\right)^{1/3}$ is the Deardorff (1970) convective velocity scale (θ_v is the virtual temperature, and h is the CBL height). A key point of (15) is employment of σ_u, $\sigma_v \sim w_*$ (Panofsky et al. 1977); that is, a convective gust is proportional to the Deardorff (1970) velocity scale w_*, which is added to the mean wind speed U. Thus, under light wind conditions (in the free-convection limit) $U \to 0$ whereas $S \to w_*$. Note that variances of the horizontal wind components in the convective surface layer are practically independent of height and, therefore, do not follow the traditional surface layer scaling.

It is obvious that vector or scalar averaging can be applied to the turbulent stress as well since the instantaneous vector of the wind stress has the same direction as the wind vector. Similar to *S* defined by Eqs. (13)-(15), the scalar averaged stress has a finite limit as U approaches zero. In this case, random CBL-scale coherent structures produce a local log-profile in the layer attached to the bottom of the large eddies. This local velocity profile generates a local stress (the 'minimum friction velocity'). Thus, the concept of gustiness immediately leads to a 'minimum friction velocity' assumption (e.g. Businger 1973; Schumann 1988; Sykes et al. 1993) also referred as the convection-induced stress regime (Grachev et al. 1997, 1998; Zilitinkevich et al. 1998, 2005, 2006). In fact, free convection can be considered as a particular case of forced convection. Zilitinkevich et al. (1998, 2005, 2006) developed a more detailed theoretical model for the non-local momentum and heat transfer. The vector or scalar averaging of the turbulent stress is related in particular to the time averaging procedure. Mahrt et al. (1996) reported a substantial difference of the drag coefficient in light winds for different averaging times and vector/scalar wind speed averaging procedures. According to Mahrt et al. (1996), higher values of the drag coefficient occur for a 10-min time averaging period compared to 60-

min averaged values. The vector averaging of the surface stress would be appropriate for determination of the average, net large scale force acting on a surface (e.g., for description of the surface currents for measurements over sea surface). Note that both the COARE and SHEBA bulk flux algorithms as well as Eq. (9) are based on the vector averaging of the turbulent stress when $\tau \propto SU$ whereas the scalar averaged wind stress assumes $\tau \propto S^2$.

Turbulent fluxes are computed from (9) – (11) and (15) via an iteration because the transfer coefficients depend on the Monin-Obukhov stability parameter z/L (L is the Obukhov length scale) which is computed from the fluxes (see Fairall et al. 1996, 2003). The forms of (9) – (11) apply well to reasonably statistically homogeneous surfaces where an interfacial value of q_0 can be unambiguously established - oceans, lakes, ice, or water-saturated soils where we can assume q_0 is the water saturation value at temperature θ_0. For dry soils and simple ground-hugging plant canopies, (9) and (10) still work but (11) does not apply. The literature is full of techniques to represent H_L for complicated situations which we will not attempt to review here (see Garratt 1992 for background). We considered a 'stomatal' resistance approach to reduce the transfer coefficient and an effective surface relative humidity to reduce the surface moisture forcing (e.g., Garratt 1992). However, to represent latent heat flux H_L we have chosen to use a Priestley and Taylor (1972, hereinafter PT) type balance (e.g., Yao et al. 2015)

$$H_L = \phi \frac{\Delta_s}{\Delta_s + \gamma} f(e)(R_{net} - G) \tag{16}$$

where Δ_s is the temperature derivative from the saturated vapor pressure relationship (see PT for detail), γ the psychrometric constant, $f(e)$ the sum of the weighted ecophysiological constraints, and ϕ the PT coefficient equal to 1.26 for a saturated surface. Note that the PT flux algorithm (16) is based on the SEB equation (1) which is assumed to be closed. The value of $f(e)$ in (16) varies from 0 to 1. According to Yao et al. (2015, Eq. 11), $f(e)$ can be expressed according to

$$f(e) = k_0 + k_1\theta_a + k_2 RH^{VPD} + (k_3 NDVI - k_4)VPD \tag{17}$$

where *VPD* is the air vapor pressure deficit $e_{sat}(\theta) - e$, *RH* the relative humidity (0 to 1), and *NDVI* the normalized difference vegetation index. The k_i (i = 0, …, 4) are empirical coefficients given in Table 1 of Yao et al. (2015) for nine different surface types. We have chosen type 'GRA' (Yao et al. 2015, their Table 1), which includes grassland and barren or sparsely vegetated soil (soil at the PS01 tower site is essentially a plowed fallow field with little vegetation).

As mentioned above, we don't have direct measurements of ground flux so we have used measurements of soil temperature and moisture to estimate G in (16) based on the Fourier's Law of Heat Conduction (8). We can integrate (8) for the interface down to some reference depth Δz, and relate the flux to the difference in the temperature at the interface to the temperature at depth Δz. Near the surface we can linearly approximate $G(z)$, so

$$\int_0^{\Delta z} \left(G + z\frac{\partial G}{\partial z}\right) dz = G\Delta z + \frac{1}{2}\frac{\partial G}{\partial z}\Delta z^2 = \lambda[\theta_0 - T_S(\Delta z)] \tag{18}$$

In this notation G in (18) is the value at the interface $z = 0$ where also $T_S(0) = \theta_0$ (cf. Eq. 10). The gradient term in (18) is estimated from the temporal change of the soil temperature

$$\rho_S c_{pS} \frac{\partial T_S}{\partial t} = -\frac{\partial G}{\partial z} \tag{19}$$

where ρ_S is the soil density and c_{pS} is the soil specific heat. Thus, G can be estimated as the sum of a gradient and storage term (Garratt 1992)

$$G = \frac{\lambda}{\Delta z}[\theta_0 - T_S(\Delta z)] + \frac{1}{2}\rho_S c_{pS}\frac{\partial T_S}{\partial t}\Delta z \tag{20}$$

The system of bulk flux computations is summarized in Table 1. Execution of these requires specification of certain coefficients which we have determined by tuning to agree with direct measurements at our site. Some other properties, such as Δ_s and γ in Eq. (16), or atmospheric stability functions, are considered universal and we take them from the literature. For the

turbulent fluxes, we need to determine the transfer coefficients C_H and C_D. Following the discussion in the Appendix, we can estimate the 10-m neutral coefficients directly via

$$C_{X10n} = \frac{\overline{w'x'}}{U_{10n}\Delta X_{10n} G_f} \tag{21}$$

Application of (21) is problematic when U_{10n} and/or ΔX_{10n} are small. We can set minimum thresholds U_{th} and ΔX_{th} for U_{10n} and ΔX_{10n} respectively and get around that by averaging (21) for a subset of the data restricted to conditions where $U_{10n} > U_{th}$ and $|\Delta X_{10n}| > \Delta X_{th}$. A variation on this approach is to do a linear regression of the form

$$\frac{\overline{w'x'}}{U_{10n} G_f} = a_x + b_x \Delta X_{10n} \tag{22}$$

so that $C_{X10n} = b_x$. This has advantages for heat flux because we do not have to restrict $\Delta\theta_{10n}$ and the offset coefficient a_x in (22) gives an indication of relative bias between θ_0 and θ_a. If there is no bias, the regression should pass through the origin; a temperature bias would be indicated as $\delta X = -a_x/b_x$. An example of normalized half-hourly averaged covariance sensible heat flux versus 10-m neutral surface-air temperature difference for the uninterrupted 30-day time series ("golden files" periods) is shown in Fig. 14 separately for dry soils (upper panel) and for wet soils (lower panel). In this case we examined fits where we have ignored observations with low wind speed (thresholds of U_{th} = 1 ms^{-1} and 4 ms^{-1} are used). The obvious outliers occur for winds less than 4 ms^{-1} but the fits yield about the same value for the Stanton number C_{H10n}, about $2.20 \cdot 10^{-3}$ using (21) and $2.15 \cdot 10^{-3}$ using (22) for dry soils (the uninterrupted 30-day time series, year days 240–270, 27 August-26 September 2016; see Fig. 10). For wet soils (the uninterrupted 30-day time series, year days 450–480, 27 25 March-24 April 2017; see Fig. 11), the corresponding values of C_{H10n} are $2.30 \cdot 10^{-3}$ using (21) and $2.39 \cdot 10^{-3}$ using (22). Similarly, results for the drag coefficient C_{D10n} are $2.76 \cdot 10^{-3}$ (21) and $2.29 \cdot 10^{-3}$ (22)

for dry soil "golden files" (year days 240–270) and $3.63 \cdot 10^{-3}$(21) and $3.21 \cdot 10^{-3}$ (22) for wet soil "golden files" (year days 450–480) for the thresholds of U_{th} = 1 ms^{-1} (plots for C_{D10n} similar to Fig. 14 are not shown here).

A similar approach can be used to determine the ground flux; for Eq. (20) we do a linear regression of the form

$$G_{res} - \frac{1}{2}\rho_S c_{pS}\frac{\partial T_S}{\partial t}\Delta z = a_g + b_g[\theta_0 - T_S(\Delta z)] \tag{23}$$

so that $\lambda/\Delta z = b_g$. Because we do not have direct measurements of G, we have substituted the residual from an assumed energy balance

$$G_{res} = R_{net} - H_S - H_L \tag{24}$$

An example for the dry soil "golden files" period (year days 240–270) and (*b*) the wet soil "golden files" period (year days 450–480) is shown in Fig. 15. Here we have plotted the individual half-hourly values (Fig. 15) and, to reduce the noise, values from the mean diurnal cycle (Fig. 16). The fit yields a value of $\lambda/\Delta z$ = 2.859 Wm^{-2}K^{-1} and 7.034 Wm^{-2}K^{-1} for dry and wet soils respectively. We have done these fits for 15-day increments throughout the experimental period and found that the thermal conductivity of the soil, λ, varies considerably but with a strong correlation to soil moisture (see discussion in Appendix 4 of Garratt 1992). This correlation is illustrated in Fig. 17. Thus, based on the data presented in Fig. 17 for the entire experimental period, we estimate λ via

$$\lambda = 0.180 + 1.09Q_{S5} \tag{25}$$

where Q_{S5} is the soil moisture measured at 5 cm depth. Of course, by tuning the coefficients to the residual flux, we are artificially forcing our parameterization to, on average, produce a reasonable total energy balance.

We also examined the use of (16) and (17) to estimate the latent heat flux H_L. We chose coefficients appropriate for bare soil from Yao et al (2015). However, we found that a constant value for the PT coefficient ϕ gave poor results. So we adjusted ϕ in (16) to give a reasonable estimate of the mean flux and, as with the soil conductivity, we fit the values to soil moisture:

$$\phi = 0.4 + 5Q_{S5} \tag{26}$$

An example comparing direct covariance and bulk estimates of the sensible and latent heat fluxes for the dry and wet soil "golden files" is shown in Fig. 18. The scatter between bulk and direct half-hour values of latent heat flux for the wet period (55%) is considerably greater than that obtained for sensible heat flux (30%) but comparable to that for ground flux (60%) for this period. The 30% scatter in the sensible heat flux (Fig. 18b) is about what we expect for covariance sampling error over half-hour averages. The additional scatter (55% vs. 30%) for latent heat flux (Fig. 18d) is likely caused by inadequacy of the model.

One further point to consider is the nature of tuning coefficients in the context of imperfect observations. If we examine (10) we see one primary coefficient C_{H10n} and three observational variables S, θ_0, and θ_a. In principle, we could tune the transfer coefficient to give the correct observed mean flux for some period. Alternatively, we could look for inconsistencies in the observables and perhaps apply a correction. It is clear that θ_0 is subject to significant error, on the order of 1°C, because it is computed from upward and downward radiative fluxes which are each uncertain by roughly 5 Wm^{-2}. Also, note that both G and $LW_{net} = LW_{down} - LW_{up}$ contain θ_0, so adjusting θ_0 will affect their mean values. Another factor is that for time periods of a few weeks, the variance of each of the fluxes is dominated by the diurnal cycle. A summary of flux statistics (monthly mean and standard deviation) for the dry and wet soil "golden files" periods is given in Tables 2 and 3 respectively. Values in Tables 2 and 3 are based on the data

presented in Fig. 18. So, if we take the mean diurnal cycle of one of the fluxes (e.g., Fig. 16), we can diagnose the relevant errors in transfer coefficients or conductivity versus biases in the observed temperatures. The strength of the diurnal cycle is principally proportional to C_{H10n} or λ. If the difference in the day-night excursions of the bulk fluxes matches the observed fluxes, then the coefficients are about right. Offsets in the mean diurnal cycles can be reduced by 'correcting' θ_0, T_S, or θ_a. For sensible heat the slope from (22) yields the transfer coefficient that will match the diurnal cycle and the intercept indicates if there is a mismatch between θ_0 and θ_a. The small intercept bias in Fig. 14 gives an indication of relatively good correlation between the sensible heat flux H_S and $\Delta\theta_{10n}$ under the assumption that θ_0 and θ_a were accurately measured. Both Figs. 15 and 16 indicate reasonable compatibility of θ_0 and T_{S5}. Thus, the bulk flux estimates provide reasonable renditions of the mean and standard deviation of the fluxes and the mean diurnal cycles (Fig. 19). The sum of the three bulk fluxes yields a reasonable balance of the net radiation at half-hour time scales (Fig. 20).

As mentioned earlier, direct measurements of the soil heat flux G with a heat flux plate were not available during the field campaign WFIP 2. However, we use model estimates of G from the bulk flux algorithm described in this section to make estimates of the SEB closure (1). Figure 21 shows the net surface energy balance based on the measured sensible and latent heat fluxes $H_S + H_L$ and bulk estimates of the ground heat flux G_b versus the net solar radiation R_{net}. Two upper panels (*a*, *b*) show incomplete the energy balance equation, $H_S + H_L$ vs. R_{net}, whereas two lower panels (*c*, *d*) are based on Eq. (1), $H_S + H_L + G_b$ vs. R_{net}. Plots in the left panels (*a*, *c*) represent the dry soil "golden files" (year days 240–270, 27 August-26 September 2016) and the right panels (*b*, *d*) represent the wet soil "golden files" period (year days 450–480, 25 March-24 April 2017). According to the data presented in Fig. 21, the SEB imbalance in the

case of the incomplete the energy balance equation, that is; $H_S + H_L$ vs. R_{net}, is about 20% for dry soils (Fig. 21a), and is about 27% for wet soils (Fig. 21b) for half-hourly averaged fluxes. However, including the bulk estimates of the ground heat flux G_b in the SEB closure equation, that is; $H_S + H_L + G_b$ vs. R_{net}, substantially reduces the SEB imbalance for each specific soil condition, (to about 5%, Fig. 21c, and 3%, Fig. 21d, respectively). The SEB imbalance is also reduced for 30-day averaged data (cf. Figs. 21a, 21b and Figs. 21c, 21d respectively). Note that plots of monthly means in Fig. 13 (triangular symbols for dry and wet soils) and in Fig. 21 (blue and pink six-pointed star symbols) are based on the data presented in Tables 2 and 3.

6 Concluding Remarks: Summary and Discussion

In this study, we present an analysis of the surface energy budget (SEB) based on field observations from the Columbia River Gorge in areas of complex terrain near Wasco, Oregon, during the 10-month long WFIP 2 field campaign. Measurements of half-hourly averaged turbulent and radiative fluxes, surface meteorology, and basic soil parameters made at the PS01 site (Figs. 1 and 2) are used to examine the SEB closure (1) for different soil conditions (dry, wet, and frozen) and at various timescales (from half-hourly to sub-annual averages). Note that similar analysis of energy closure variation over different temporal scales in the literature is rare.

These estimates of the SEB (1) are generally consistent with past eddy-covariance results over land showing that at half-hourly resolution the sum of turbulent fluxes of sensible and latent heat typically under balance the positive net radiation by about 20-30% during daytime and overestimate negative net radiation at night (Fig. 7a). We note that SEB-imbalance is a longstanding issue in micro-meteorology. However, increasing averaging time from half-hourly

to longer intervals (i.e., to daily, monthly, and sub-annual timescales) substantially reduces the SEB imbalance (Fig. 7b) and, additionally, the longer averaging times can reduce the influence of instrumental measurement errors (e.g. improper calibration) and sampling uncertainties. We find the SEB can be closed for this site within reasonable limits on sub-annual timescales (311-day averaging for the entire field campaign dataset).

At all averaging timescales, the SEB closure was lower for wet soils compared to dry soils while closure for frozen soils appears weak, if not non-existent (Fig. 13), likely due to the lack of a latent heat of fusion term in the SEB equation (1). However, the latent heat of fusion term is not significant at annual (or sub-annual) timescales because, on average, heat absorbed from the atmosphere during the spring thaw is subsequently released during the fall freeze. This is a temporal redistribution of energy in the top soil layer due to the water/ice-phase transition of the annual freeze–thaw cycle. The SEB can be closed for dry soil within about two percent on seasonal timescale (81-day) over the entire dataset (Figs. 9a and 13) and even on a daily timescale for month-long uninterrupted data records ("golden files", Fig. 10).

The purpose of this study is not closure of the SEB at half-hourly time scales (or forcing SEB closure based on the direct measurements of all SEB components), but rather, to evaluate SEB closure over a range of timescales and derive a bulk flux algorithm. The problem of surface energy imbalance and the individual factors (e.g., storage terms) that lead to the imbalance at half-hourly and hourly time scales has been widely investigated in many studies (e.g., references in Section 2). Here, we analyze and discuss the balance between net radiation and turbulent sensible and latent heat fluxes. Direct measurements of the soil heat flux were not available, which may be seen as a disadvantage, but in many numerical climate models only the net radiation and sensible/latent heat fluxes are used to determine the surface temperature. Thus,

SEB closure for these fluxes (Fig. 13) is important. Nevertheless, complete closure is possible at half-hourly and hourly averaged time scales by accurate determination of all SEB components (turbulent, radiative, ground heat fluxes and storage energy terms) and careful attention to all sources of measurement and data processing errors (e.g., Lamaud et al. 2001; Jacobs et al. 2008; Leuning et al. 2012).

Uninterrupted time series ("golden files") for dry and wet soils (described in Section 4.4) are used to develop a bulk flux algorithm for predicting the surface fluxes from more readily measured or modelled quantities (Section 5). The bulk flux algorithm consists of (i) the traditional COARE bulk flux algorithm (Fairall et al. 1996, 2003) for estimation of the surface turbulent fluxes of momentum τ and the sensible heat H_S, and (ii) a modified Priestley-Taylor (PT) model by Yao et al. (2015) to estimate the latent heat flux H_L based on the measured soil moisture and temperature. Including the bulk estimates of the ground heat flux G_b in the SEB closure equation substantially reduces the SEB imbalance for each specific soil condition as compared to the incomplete the energy balance equation, $H_S + H_L$ versus R_{net} (Fig. 21).

Acknowledgements This work is supported by the NOAA Atmospheric Science for Renewable Energy Program, NOAA/Earth System Research laboratory/Physical Sciences Division, and by the U.S. Department of Energy (DoE) DE-EE0007605 interagency agreement that supports DoE FOA DE-FOA-0000984. The University of Notre Dame team was supported by DOE-WFIFP2-SUB-001. Thanks go to Ola Persson for the helpful comments and suggestions on improving the manuscript.

Appendix: Turbulent flux algorithm

This is described in detail in Fairall et al. (1996, 2003) but is sketched here. The bulk variables are used to compute so-called Monin-Obukhov (MO) scaling parameters

$$x_* = -c_x \Delta X \tag{A1}$$

where $x = u$, θ, or q, $X = U$, θ, or q, and $\Delta X = X_0 - X_a$ is the difference between the surface value (zero for wind speed U) and the value at reference height z in the atmosphere

$$c_x = \frac{C_x}{C_D^{1/2}} \tag{A2}$$

The scaling parameters yield the turbulent covariance by

$$\overline{w'x'} = -u_* x_* G_f \tag{A3}$$

with $G_f = S/U$ called the gustiness factor. Traditionally, the transfer coefficients (A2) are adjusted to neutral conditions using MO similarity theory via

$$c_x = \frac{c_{xn}}{1 - \frac{c_{xn}}{\kappa}\Psi_x(\zeta)} \tag{A4}$$

Here $\Psi_x(\zeta)$ are the MO stability functions for mean profiles of x in the surface layer. In neutral conditions ($\zeta \equiv 0$) the Ψ-functions obey $\Psi_x(0) = 0$. Subscript n in c_{xn} in (A4) denotes the value in neutral conditions. The MO stability parameter $\zeta = z/L$ (L is the Obukhov length) is defined by

$$\zeta = \frac{\kappa g z}{\theta_a} \frac{\theta_{v*}}{u_*^2} \tag{A5}$$

Here g is the acceleration due to gravity and, historically, the von Kármán constant $\kappa \approx 0.4$ is included in the definition of L and ζ simply by convention. Subscript v in θ_{v*} in (A5) denotes the

virtual temperature. The neutral transfer coefficients in (A4) are uniquely related to the aerodynamic roughness lengths z_{0x} through

$$c_{xn} = \frac{\kappa}{\log(z/z_{0x})} \tag{A6}$$

The transfer coefficients depend on height via (A6) but the roughness lengths are fixed for a given surface. Transfer coefficients for operational or practical considerations are usually represented at a standard reference height of 10 m and neutral conditions. In this regard, the turbulent kinematic fluxes can be written in terms of mean quantities as

$$\overline{w'x'} = C_{X10n} U_{10n} \Delta X_{10n} G_f \tag{A7}$$

where the 10-m neutral bulk values are given by

$$\Delta X_{10n} = \frac{\Delta X}{1 + c_{x10n}[\log(z/10) - \Psi_x(\zeta)]} \tag{A8}$$

References

Andreas E.L, Horst T.W., Grachev A.A., Persson P.O.G., Fairall C.W., Guest P.S., Jordan R.E. (2010a) Parametrizing turbulent exchange over summer sea ice and the marginal ice zone. *Quart. J. Roy. Meteorol. Soc.* **136**(649B), 927–943. DOI: 10.1002/qj.618

Andreas E.L, Persson P.O.G., Jordan R.E., Horst T.W., Guest P.S., Grachev A.A., Fairall C.W. (2010b) Parameterizing turbulent exchange over sea ice in winter. *J. Hydrometeorol*. **11**(1), 87–104. DOI: 10.1175/2009JHM1102.1

Arya P.S. (1988) *Introduction to Micrometeorology*, Academic Press, San Diego, 307 pp

Bariteau L., Helmig D., Fairall C.W., Hare J.E., Hueber J., Lang E.K. (2010) Determination of oceanic ozone deposition by ship-borne eddy covariance flux measurements. *Atmos. Meas. Tech*. **3**(2): 441–455. DOI: 10.5194/amt-3-441-2010

Blomquist B.W., Huebert B.J., Fairall C.W., Bariteau L., Edson J.B., Hare J.E., McGillis W.R. (2014) Advances in air-sea CO_2 flux measurement by eddy correlation. *Boundary-Layer Meteorol*. **152**(3): 245–276. DOI: 10.1007/s10546-014-9926-2

Businger J.A. (1973) A note on free convection. *Boundary-Layer Meteorol*. **4**(1-4): 323–326. DOI: 10.1007/BF02265241

Cava D., Contini D., Donateo A., Martano P. (2008) Analysis of short-term closure of the surface energy balance above short vegetation. *Agric. Forest Meteorol*. **148**(1): 82–93. DOI: 10.1016/j.agrformet.2007.09.003

Cuxart J., Conangla L., Jiménez M.A. (2015) Evaluation of the surface energy budget equation with experimental data and the ECMWF model in the Ebro Valley. *J. Geophys. Res. Atmos*. **120**(D3): 1008–1022. DOI: 10.1002/2014JD022296.

Deardorff J.W. (1970) Convective velocity and temperature scales for the unstable planetary boundary layer and for Rayleigh convection. *J. Atmos. Sci*. **27**(8): 1211–1213

Ezzahar J., Er-Raki S., Marah H., Khabba S., Amenzou N., Chehbouni G. (2012) Coupling soil-vegetation-atmosphere-transfer model with energy balance model for estimating energy and water vapor fluxes over an olive grove in a semi-arid region. *Global Meteorol*. **1**, 10.4081/gm.2012.e1

Fairall C.W., Bradley E.F., Rogers D.P., Edson J.B., Young G.S. (1996) Bulk parameterization of air-sea fluxes for Tropical Ocean - Global Atmosphere Coupled-Ocean Atmosphere Response Experiment. *J. Geophys. Res.* **101**(C2): 3747–3764. DOI: 10.1029/95JC03205

Fairall C.W., Bradley E.F., Hare J.E., Grachev A.A., Edson J.B. (2003) Bulk parameterization of air-sea fluxes: updates and verification for the COARE algorithm. *Journal of Climate*, **16**(4), 571–591.

Finnigan J. (2008) An introduction to flux measurements in difficult conditions. *Ecological Applications*, **18**(6): 1340–1350. DOI: 10.1890/07-2105.1

Foken T., Oncley S.P. (1995) Results of the workshop "Instrumental and methodical problems of land surface flux measurements". Bull. Am. Meteorol. Soc. 76(7): 1191–1193

Foken T., Wimmer F., Mauder M., Thomas C., Liebethal C. (2006) Some aspects of the energy balance closure problem. *Atmos. Chem. Phys*. **6**(12): 4395–4402. DOI: 10.5194/acp-6-4395-2006

Foken T. (2008) The energy balance closure problem: An overview. *Ecological Applications*, **18**(6): 1351–1367. DOI: 10.1890/06-0922.1

Gao Z., Horton R., Liu H.P. (2010) Impact of wave phase difference between soil surface heat flux and soil surface temperature on soil surface energy balance closure. *J. Geophys. Res*. **115**(D16): D16112. DOI: 10.1029/2009JD013278

Gao Z., Liu H., Katul G.G., Foken T. (2017) Non-closure of the surface energy balance explained by phase difference between vertical velocity and scalars of large atmospheric eddies. *Environ. Res. Lett*. **12**(3): 034025. DOI: 10.1088/1748-9326/aa625b

Garratt J.R. (1992) *The Atmospheric Boundary Layer.* Cambridge University Press, U.K. 316 pp

Grachev A.A., Fairall C.W., Zilitinkevich S.S. (1997) Surface-layer scaling for the convection-induced stress regime. *Boundary-Layer Meteorol*. **83**(3), 423–439. DOI: 10.1023/A:1000281625985

Grachev A.A., Fairall C.W., Larsen S.E. (1998) On the determination of the neutral drag coefficient in the convective boundary layer. *Boundary-Layer Meteorol*. **86**(2): 257–278. DOI: 10.1023/A:1000617300732

Grachev A.A., Fairall C.W., Persson P.O.G., Andreas E.L, Guest P.S. (2005) Stable boundary-layer scaling regimes: the SHEBA data. *Boundary-Layer Meteorol.* **116**(2): 201–235. DOI 10.1007/s10546-004-2729-0

Grachev A.A., Bariteau L., Fairall C.W., Hare J.E., Helmig D., Hueber J., Lang E.K. (2011) Turbulent fluxes and transfer of trace gases from ship-based measurements during TexAQS 2006. *J. Geophys. Res.* **116**: D13110. DOI: 10.1029/2010JD015502

Grachev A.A., Persson P.O.G., Uttal T., Akish E.A., Cox C.J., Morris S.M., Fairall C.W., Stone R.S., Lesins G., Makshtas A.P., Repina I.A. (2018) Seasonal and latitudinal variations of surface fluxes at two Arctic terrestrial sites. *Climate Dynamics*. **51**(5-6): 1793–1818. DOI: 10.1007/s00382-017-3983-4

Higgins C.W. (2012) A-posteriori analysis of surface energy budget closure to determine missed energy pathways. *Geophys. Res. Lett*. **39**(19): L19403. DOI: 10.1029/2012GL052918

Jacobs A.F.G., Heusinkveld B.G., Holtslag A.A.M. (2008) Towards closing the surface energy budget of a mid-latitude grassland. *Boundary-Layer Meteorol*. **126**(1): 125–136. DOI: 10.1007/s10546-007-9209-2

Kustas W.P.,Daughtry C.S.T. (1990) Estimation of the soil heat flux/net radiation ratio from spectral data. *Agric. Forest Meteorol*. **49**(3): 205–223. DOI: 10.1016/0168-1923(90)90033-3

Kustas W.P., Daughtry C.S.T., Van Oevelen P.J. (1993) Analytical treatment of the relationship between soil heat flux/net radiation ratio and vegetation indices. *Remote Sens. Environ*. **46**(3): 319–330. DOI: 10.1016/0034-4257(93)90052-Y

Kustas W.P., Norman J.M., Schmugge T.J., Anderson M.C. (2004) Mapping surface energy fluxes with radiometric temperature. In: D.A. Quattrochi, J.C. Luvall (eds.) *Thermal remote sensing in land surface processes*. Boca Raton, Florida: CRC Press, 2004, p. 205–253.

Lamaud E., Ogée J., Brunet Y., Berbigier P. (2001) Validation of eddy flux measurements above the understorey of a pine forest. *Agric. Forest Meteorol*. **106**(3): 187–203. DOI: 10.1016/S0168-1923(00)00215-X

Lettau H., Davidson B. (1957) Exploring the atmosphere's first mile. Vol. I. *Instrumentation and data evaluation*. Pergamon Press, New York.

Leuning R., van Gorsel E., Massman W.J., Isaac P.R. (2012) Reflections on the surface energy imbalance problem. *Agric. Forest Meteorol*. **156**: 65–74. DOI: 10.1016/j.agrformet.2011.12.002

Long I.F., Monteith J.L., Penman H.L., Szeicz G. (1964) The plant and its environment. *Meteorol. Rundsch*. **17**: 97–101

Mahrt L., Vickers D., Howell J., Højstrup J., Wilczak J. M., Edson J., Hare J. (1996) Sea surface drag coefficients in the Risø Air Sea Experiment. *J. Geophys. Res*. **101**(C6): 14,327–14,335. DOI: 10.1029/96JC00748

Majozi N.P., Mannaerts C.M., Ramoelo A., Mathieu R., Nickless A., Verhoef W. (2017) Analysing surface energy balance closure and partitioning over a semi-arid savanna FLUXNET site in Skukuza, Kruger National Park, South Africa. *Hydrol. Earth Syst. Sci*. **21**(7): 3401–3415. DOI: 10.5194/hess-21-3401-2017

Mauder M., Oncley S.P., Vogt R., Weidinger T., Ribeiro L., Bernhofer C., Foken T., Kohsiek W., De Bruin H.A.R., Liu H. (2007) The Energy Balance Experiment EBEX-2000. Part II: Intercomparison of eddy-covariance sensors and post-field data processing methods. *Boundary Layer Meteorol*. **123**(1): 29–54. DOI: 10.1007/s10546-006-9139-4

Masseroni D., Corbari C., Mancini M. (2014) Limitations and improvements of the energy balance closure with reference to experimental data measured over a maize field. *Atmósfera*, **27**(4): 335–352. DOI: 10.1016/S0187-6236(14)70033-5

Meyers T.P., S.E. Hollinger (2004) An assessment of storage terms in the surface energy balance of maize and soybean. *Agric. Forest Meteorol*. **125**(1-2): 105–115. DOI: 10.1016/j.agrformet.2004.03.001

Nobel P.S. (1991) *Physicochemical and Environmental Plant Physiology*. Fourth Edition, Elsevier Academic Press, Oxford UK, 582p.

Panin G.N., Bernhofer C. (2008) Parametrization of turbulent fluxes over inhomogeneous landscapes. *Izvestiya, Atmos. Ocean. Phys*. **44**(6): 701–716. DOI: 10.1134/S0001433808060030

Panofsky H.A., Tennekes H., Lenschow D.A., Wyngaard J.C. (1977) The characteristics of turbulent velocity components in the surface layer under convective conditions. *Boundary-Layer Meteorol.* **11**(3): 355–361. DOI: 10.1007/BF02186086

Priestley C. and Taylor R. (1972) On the assessment of surface heat flux and evaporation using large-scale parameters. *Mon. Wea. Rev*. **100**(2): 81–92.

Reed D.E., Frank J.M., Ewers B.E., Desai A.R. (2018) Time dependency of eddy covariance site energy balance. *Agric. Forest Meteorol*. **249**: 467-478. DOI: 10.1016/j.agrformet.2017.08.008.

Roxy M.S., Sumithranand V.B., Renuka, G. (2014) Soil heat flux and day time surface energy balance closure at astronomical observatory, Thiruvananthapuram, south Kerala. *J. Earth Syst. Sci*. **123**(4): 741–750. DOI: 10.1007/s12040-014-0437-9

Sauer T.J., Hatfield J.L., Prueger J.H., Norman J.M. (1998) Surface energy balance of a corn residue-covered field. *Agric. Forest Meteorol*. **89**(3–4): 155–168. DOI: 10.1016/S0168-1923(97)00090-7

Schumann U. (1988) Minimum friction velocity and heat transfer in the rough surface layer of a convective boundary layer. *Boundary-Layer Meteorol*. **44** (4): 311–326. DOI: 10.1007/BF00123019

Stone R.S., Dutton E.G., Harris J.M., Longenecker D. (2002) Earlier spring snowmelt in northern Alaska as an indicator of climate change, *J. Geophys. Res*. **107**(D10): 4089. DOI: 10.1029/2000JD000286

Stoy P.C., Mauder M., Foken T., Marcolla B., Boegh E., Ibrom A., Arain M.A., Arneth A., Aurela M., Bernhofer C., Cescatti A., Dellwik E., Duce P., Gianelle D., van Gorsel E., Kiely G., Knohl A., Margolis H., McCaughey H., Merbold L., Montagnani L., Papale D.,

Reichstein M., Saunders M., Serrano-Ortiz P., Sottocornola M., Spano D., Vaccari F., Varlagin A. (2013) A data-driven analysis of energy balance closure across FLUXNET research sites: The role of landscape scale heterogeneity. *Agric. Forest Meteorol*. **171-172**: 137–152. DOI: 10.1016/j.agrformet.2012.11.004

Su Z.(2002) The Surface Energy Balance System (SEBS) for estimation of turbulent heat fluxes. *Hydrol. Earth Syst. Sci*. **6**(1) 85-100. DOI: 10.5194/hess-6-85-2002,

Sun T., Wang Z.-H., Ni G.-H. (2013) Revisiting the hysteresis effect in surface energy budgets. *Geophys. Res. Lett*. **40**(9): 1741–1747. DOI: 10.1002/grl.50385

Sykes R.I., Henn D.S., Lewellen W.S. (1993) Surface-layer description under free-convection conditions. *Quart. J. Roy. Meteorol. Soc*. **119**(511): 409–421. DOI: 10.1002/qj.49711951103

Wilson K., Goldstein A., Falge E., Aubinet M., Baldocchi D., Berbigier P., Bernhofer C., Ceulemans R., Dolman H., Field C., Grelle A., Ibrom A., Law B.E, Kowalski A., Meyers T., Moncrieff J., Monson R., Oechel W., Tenhunen J., Valentini R., Verma S. (2002) Energy balance closure at FLUXNET sites. *Agric. Forest Meteorol*. **113**(1-4): 223–243. DOI: 10.1016/S0168-1923(02)00109-0

Wilczak J.M., Oncley S.P., Stage S.A. (2001) Sonic anemometer tilt correction algorithms. *Boundary-Layer Meteorol.* **99**(1): 127–150. DOI: 10.1023/A:1018966204465

Yao Y., Liang S., Li X., Chen J., Wang K., Jia K., Cheng J., Jiang B., Fisher J.B., Mu Q., Grünwald T., Bernhofer C., Roupsard O. (2015) A satellite-based hybrid algorithm to determine the Priestley-Taylor parameter for global terrestrial latent heat flux estimation across multiple biomes. *Remote Sens. Environ*. **165**: 216–233. DOI: 10.1016/j.rse.2015.05.013

Zilitinkevich S.S., Grachev A.A., Hunt J.C.R. (1998) Surface frictional and non-local heat/mass transfer in the shear-free convective boundary layer, in *Buoyant Convection in Geophysical Flows* (Plate E.J., Fedorovich E.E., Viegas D.X., Wyngaard J.C., Eds.), NATO ASI Series, Kluwer, 83–113.

Zilitinkevich S.S., Hunt J.C.R., Grachev A.A., Esau I.N., Lalas D.P., Akylas E., Tombrou M., Fairall C.W., Fernando H.J.S., Baklanov A., Joffre S.M. (2005) The effect of large eddies on the convective heat/mass transfer over complex terrain: advanced theory and its validation against experimental and les data. *Croatian Meteorological Journal*. **40**, 20–26.

Zilitinkevich S.S., Hunt J.C.R., Esau I.N., Grachev A.A., Lalas D.P., Akylas E., Tombrou M., Fairall C.W., Fernando H.J.S., Baklanov A.A., Joffre S.M. (2006) The influence of large convective eddies on the surface layer turbulence. *Quart. J. Roy. Met. Soc.*, **132**(618A), 1423–1456. DOI: 10.1256/qj.05.79

Table 1. Summary of bulk flux calculation relationships

Flux Variables	Equation	Coefficients	Input Variables
$\tau,\ H_S$	(9), (10), (15)	C_D, C_H	$U, \theta_0, \theta_a, q_a$
H_L	(16), (17)	ϕ, k_i	R_{net}, G
G	(20)	λ, ρ_S, c_{pS}	θ_0, T_{S5}

Table 2. Summary of flux statistics (monthly averages and standard deviations) for the dry soil "golden files" (year days 240–270)

Flux Variables	<Bulk>	<Direct>	σ Bulk	σ Direct
$G\ [Wm^{-2}]$	-2.4		58.9	
$H_S\ [Wm^{-2}]$	71.5	69.9	131.2	126.9
$H_L\ [Wm^{-2}]$	9.0	7.4	20.0	22.3
$\tau\ [Nm^{-2}]$	0.10	0.12	0.11	0.13
$R_{net}\ [Wm^{-2}]$		72.8		173.0

Table 3. Summary of flux statistics (monthly averages and standard deviations) for the wet soil "golden files" (year days 450–480)

Flux Variables	<Bulk>	<Direct>	σ Bulk	σ Direct
$G\ [Wm^{-2}]$	7.4		66.4	
$H_S\ [Wm^{-2}]$	40.0	40.2	87.4	88.0
$H_L\ [Wm^{-2}]$	45.7	53.3	68.1	61.2
$\tau\ [Nm^{-2}]$	0.13	0.15	0.16	0.19
$R_{net}\ [Wm^{-2}]$		108.9		201.9

Figure Captions

Figure 1. Maps showing the WFIP 2 study area located along the Columbia River Gorge in eastern Oregon and Washington states.

Figure 2. View of the flux tower and instruments at the WFIP 2 Physics site PS01 during late summer conditions (15 September 2016).

Figure 3. Time series of (*a*) wind speed, (*b*) true wind direction, (*c*) air temperature, and (*d*) relative humidity for year days 176–487 (24 June 2016-01 May 2017) observed at Columbia River Gorge, OR during WFIP 2 Project (Physics site PS01). The data are based on half-hour averaging.

Figure 4. Time series of (*a*) soil temperature and (*b*) soil moisture observed at the WFIP 2 Physics site PS01, and (*c*) rain rate observed near the Wasco State Airport, OR (WCO) for year days 176–487 (24 June 2016-01 May 2017). The data are based on half-hour averaging.

Figure 5. Time series of (*a*) short-wave (SW) downwelling and upwelling radiation, (*b*) long-wave (LW) downwelling and upwelling radiation, (*c*) SW balance, LW balance, and net radiation, and (*d*) albedo for year days 176–487 (24 June 2016-01 May 2017) observed at Columbia River Gorge, OR during WFIP 2 Project. The data are based on half-hour and daily averaging.

Figure 6. Time series of (a) friction velocity observed at 3 and 10 m, (b) sensible heat flux observed at 3 and 10 m, and (c) latent heat (water vapor) flux for year days 176–487 (24 June 2016-01 May 2017) observed at Columbia River Gorge, OR during WFIP 2 Project. The data are based on half-hour averaging.

Figure 7. Scatter plots of the sum of the sensible and latent heat fluxes $H_S + H_L$ versus the net solar radiation R_{net} based on (a) the half-hourly averaged (symbols) and the bin-averaged (solid line) data and (b) the daily, monthly and 311-day (the entire dataset) averaged fluxes for the entire dataset collected at Columbia River Gorge, OR during WFIP 2 Project during year days 176–487 (24 June 2016-01 May 2017).

Figure 8. Plots of the bin-averaged (solid lines) and 0.5-hr averaged (symbols) turbulent fluxes (eddy-covariance) of (a) sensible heat H_S, (b) latent heat H_L, and (c) the sum $H_S + H_L$ (SEB turbulent flux components) versus the net solar radiation R_{net} for dry, wet, and frozen soils observed at Columbia River Gorge, OR during WFIP 2 Project during year days 176–487 (24 June 2016-01 May 2017).

Figure 9. Plots of the sum of the sensible and latent heat fluxes $H_S + H_L$ versus the net solar radiation R_{net} separately for (a) dry, (b) wet, and (c) frozen (snow covered) soils based on daily averaged fluxes and entire dataset averaging (81, 92, and 58-day averaging in each case respectively).

Figure 10. One-month (30-day) time series of (a) the net solar radiation R_{net}, (b) the sum of the sensible and latent heat fluxes $H_S + H_L$, (c) the residual energy $R_{net} - H_S - H_L$ and (d) difference of the soil temperature between 10 cm and 5 cm levels for dry soils observed at the WFIP 2 Physics site PS01 during year days 240–270 (27 August-26 September 2016). The data are based on half-hour and daily averaging.

Figure 11. Same as Fig. 10 but for wet soils observed at the WFIP 2 Physics site PS01 during year days 450–480 (25 March-24 April 2017). The data are based on half-hour and daily averaging.

Figure 12. Same as Fig. 10 but for frozen (snow covered) soils observed at the WFIP 2 Physics site PS01 during year days 395–425 (29 January-28 February 2017). The data are based on half-hour and daily averaging.

Figure 13. The surface energy balance (SEB) closure at different temporal scales: ratio of turbulent energy fluxes $H_S + H_L$ to net solar radiation R_{net} for the entire dataset (red solid line and red symbols) and separately for different soil types plotted versus averaging time based on the data collected at Columbia River Gorge, OR during WFIP 2 Project.

Figure 14. Linear regression fit of normalized half-hourly averaged covariance sensible heat flux versus 10-m neutral surface-air temperature difference for (a) the dry soil "golden files" (year days 240–270, 27 August-26 September 2016) and (b) the wet soil "golden files" period (year days 450–480, 25 March-24 April 2017). The green ×-symbols are data for 10-m neutral wind

speed greater than 1 ms^{-1}; for blue +-symbols only wind speed greater than 4 ms^{-1} are considered.

Figure 15. Storage term adjusted ground flux (residual) versus temperature difference between surface (θ_0) and soil at 5 cm depth (T_{S5}) for (*a*) the dry soil "golden files" period (year days 240–270) and (*b*) the wet soil "golden files" period (year days 450–480). The green ×-symbols are half-hourly averaged values; blue circles are derived from the mean diurnal cycle. The magenta solid line is a regression with $\lambda/\Delta z = 2.859 Wm^{-2}K^{-1}$ for the dry soils and $\lambda/\Delta z = 7.034 Wm^{-2}K^{-1}$ for the wet soils.

Figure 16. Mean diurnal plot of ground flux G for (*a*) the dry soil "golden files" period (year days 240–270) and (*b*) the wet soil "golden files" period (year days 450–480). The blue lines are the residual estimate of G and the red lines are G computed via (20).

Figure 17. Regression fit of the thermal conductivity of the soil λ versus soil moisture content at 5 cm depth Q_{S5}, see Eq. (25).

Figure 18. Scatter plots of the bulk estimates of (*a*, *b*) sensible heat flux H_S and (*c*, *d*) latent heat flux H_L versus their measured (direct covariance) counterparts based on the half-hourly averaged data using (16) and (17) with $\phi = 0.4 + 5Q_{S5}$ (ϕ not to exceed 1.45). Plots in the left panels (*a*, *c*) represent the dry soil "golden files" (year days 240–270) and the right panels (*b*, *d*) represent the wet soil "golden files" period (year days 450–480).

Figure 19. Mean diurnal cycle of sensible, latent, and ground heat fluxes for (*a*) dry and (*b*) wet soil "golden files" periods. Direct measurements are solid lines with triangle symbols; the bulk estimates are dashed lines with circle symbols.

Figure 20. Net surface energy balance from bulk flux calculations for (*a*) the dry soil "golden files" (year days 240–270) and (*b*) the wet soil "golden files" period (year days 450–480). Observed net radiation R_{net} versus the sum of the sensible, latent and ground fluxes as yielded by (10), (16), and (20).

Figure 21. Scatter plots of the net surface energy balance for (*a*, *b*) the sum of the measured sensible and latent heat fluxes $H_S + H_L$ and (*c*, *d*) the sum of the measured $H_S + H_L$ and bulk estimates of the ground heat flux G_b versus the net solar radiation R_{net} based on the half-hourly and monthly averaged data. Plots in the left panels (*a*, *c*) represent the dry soil "golden files" (year days 240–270) and the right panels (*b*, *d*) represent the wet soil "golden files" period (year days 450–480).

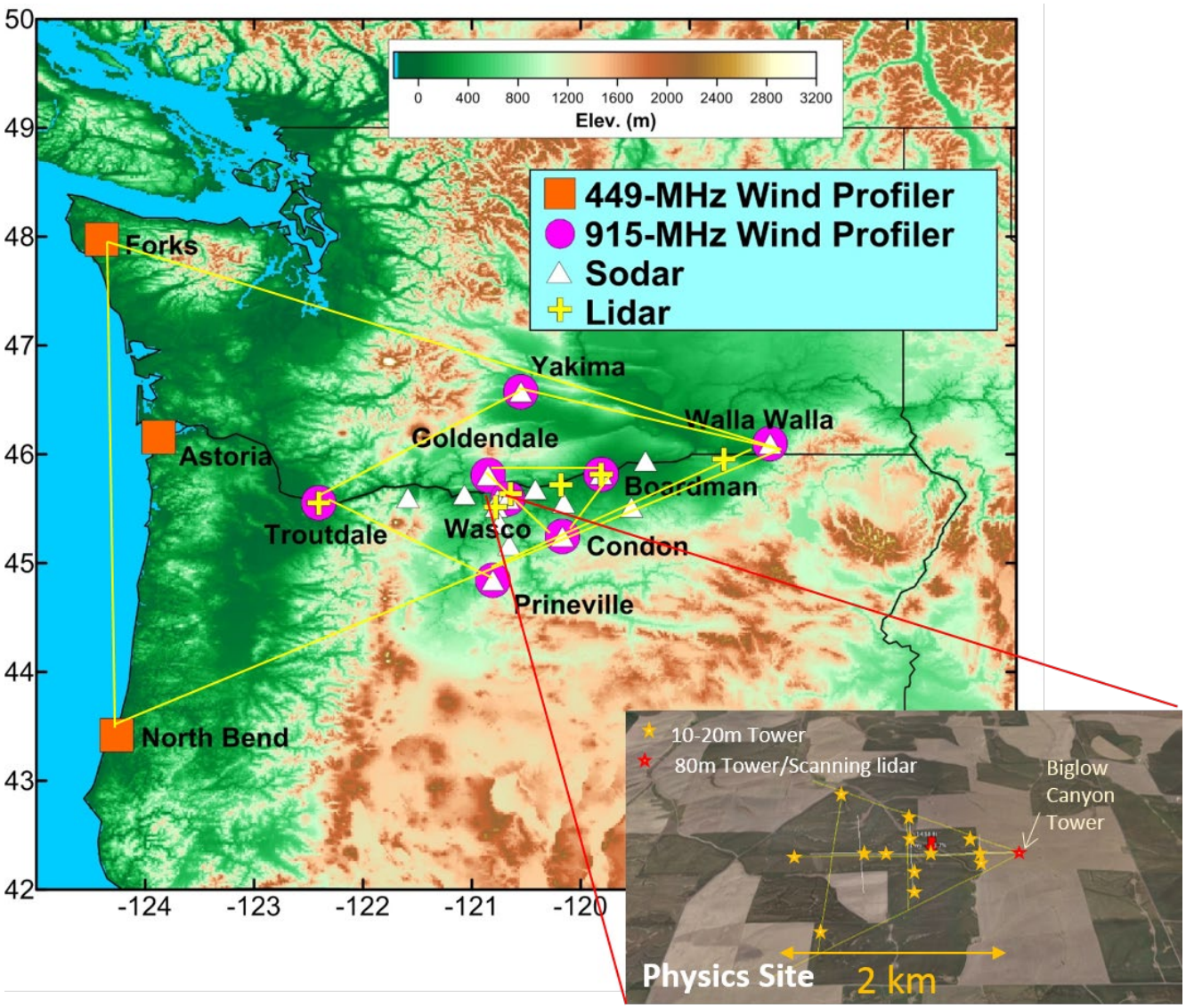

Figure 1. Maps showing the WFIP 2 study area located along the Columbia River Gorge in eastern Oregon and Washington states.

Figure 2. View of the flux tower and instruments at the WFIP 2 Physics site PS01 during late summer conditions (15 September 2016).

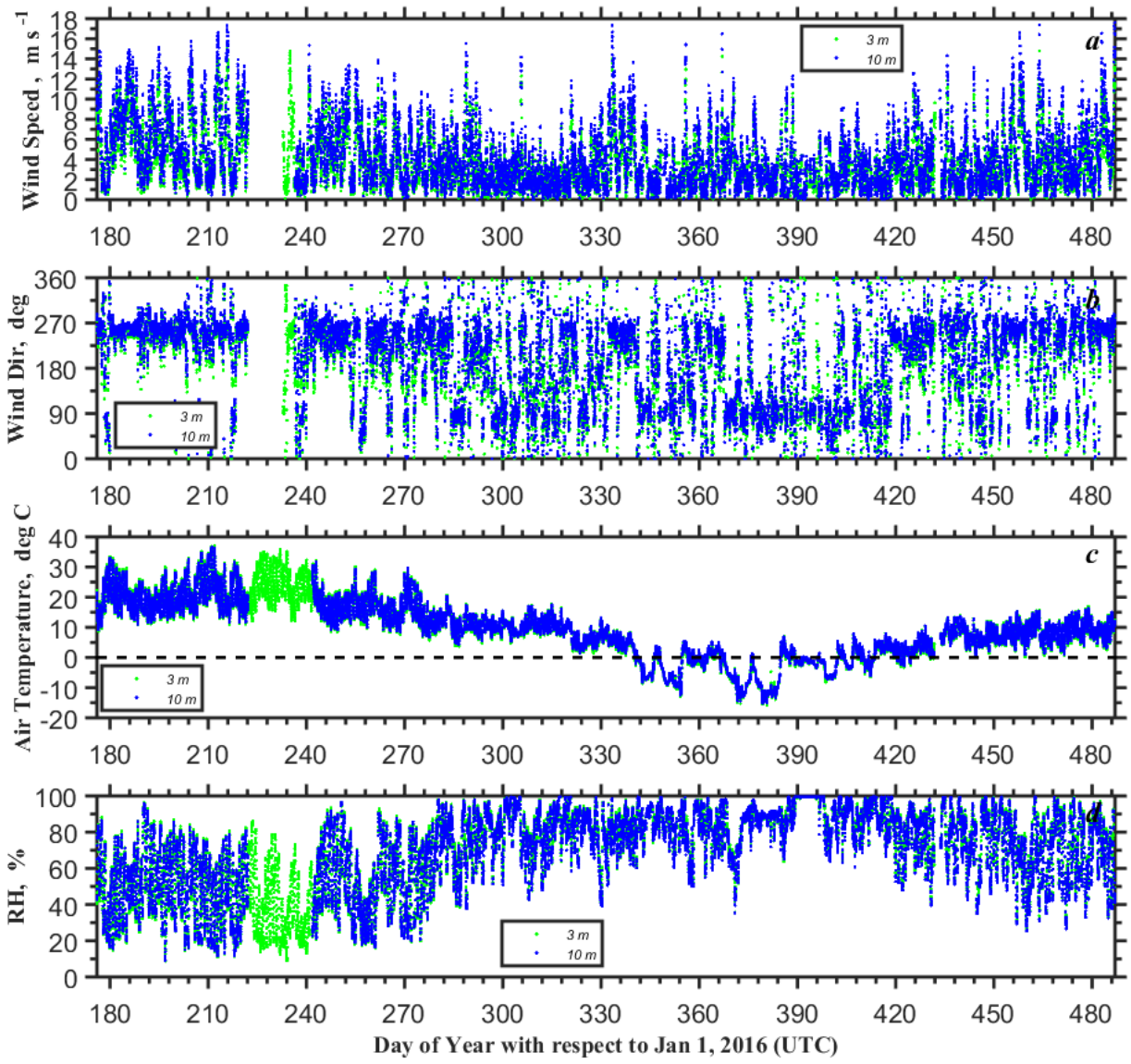

Figure 3. Time series of (*a*) wind speed, (*b*) true wind direction, (*c*) air temperature, and (*d*) relative humidity for year days 176–487 (24 June 2016-01 May 2017) observed at Columbia River Gorge, OR during WFIP 2 Project (Physics site PS01). The data are based on half-hour averaging.

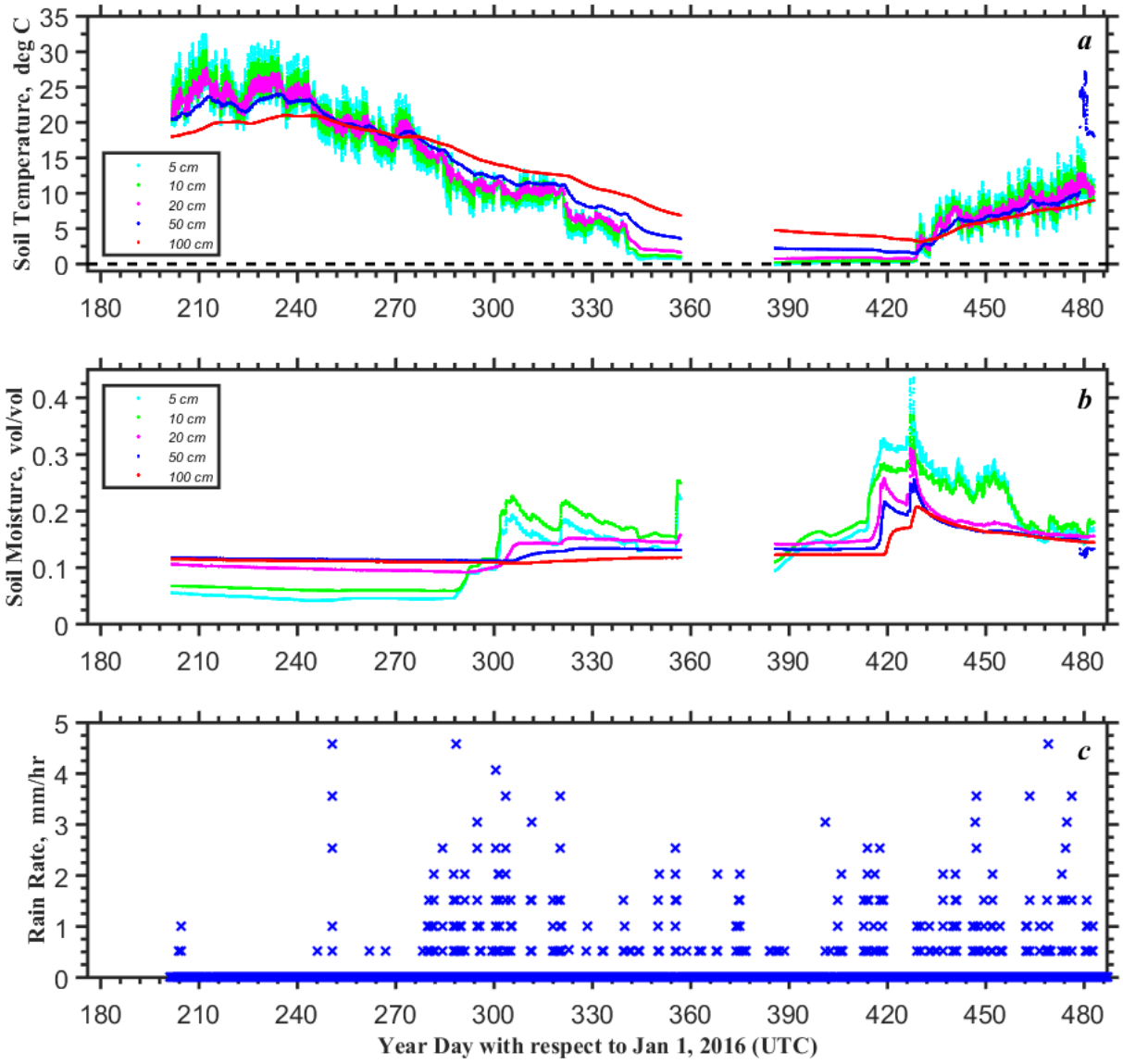

Figure 4. Time series of (*a*) soil temperature and (*b*) soil moisture observed at the WFIP 2 Physics site PS01, and (*c*) rain rate observed near the Wasco State Airport, OR (WCO) for year days 176–487 (24 June 2016-01 May 2017). The data are based on half-hour averaging.

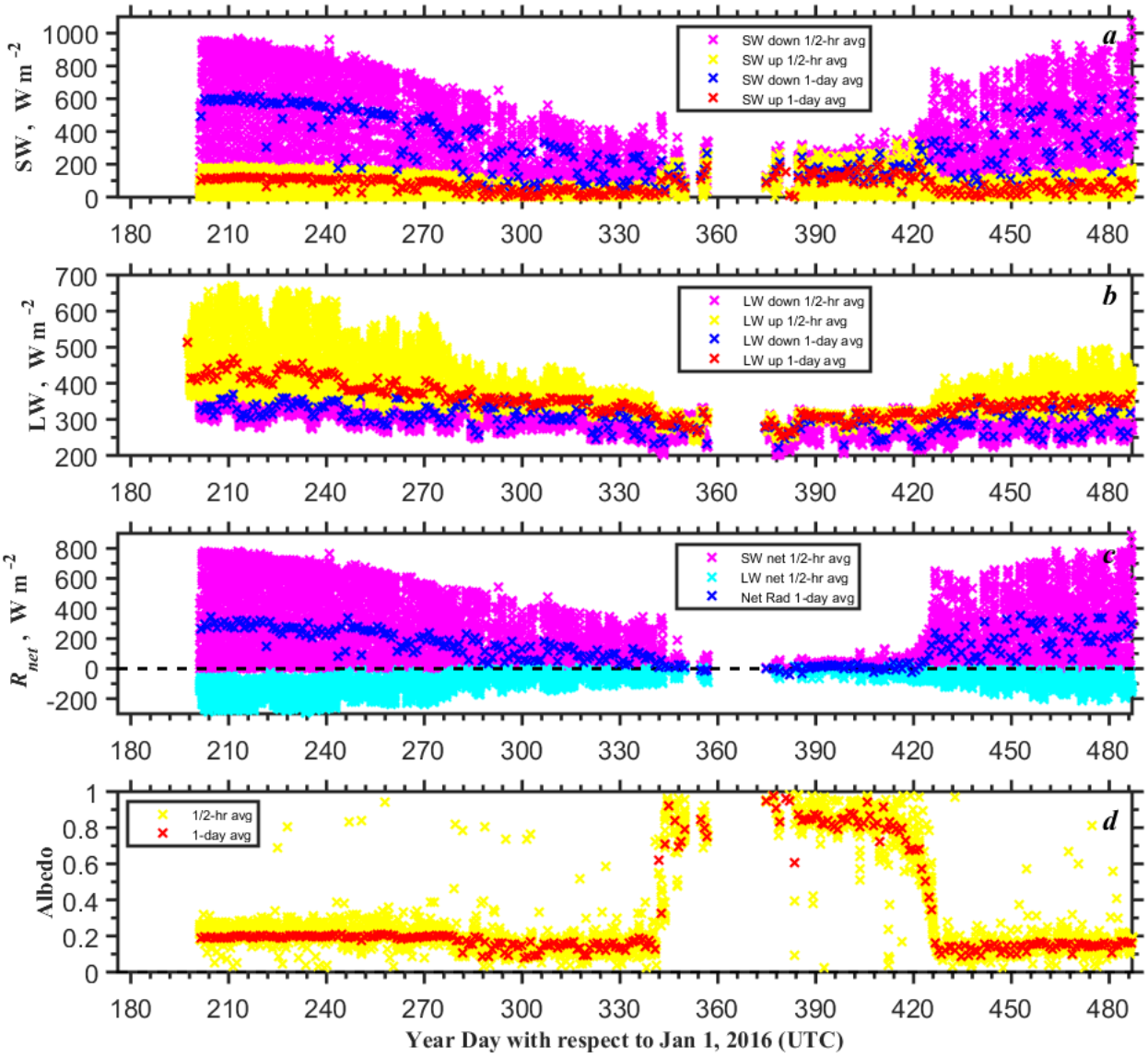

Figure 5. Time series of (*a*) short-wave (SW) downwelling and upwelling radiation, (*b*) long-wave (LW) downwelling and upwelling radiation, (*c*) SW balance, LW balance, and net radiation, and (*d*) albedo for year days 176–487 (24 June 2016-01 May 2017) observed at Columbia River Gorge, OR during WFIP 2 Project. The data are based on half-hour and daily averaging.

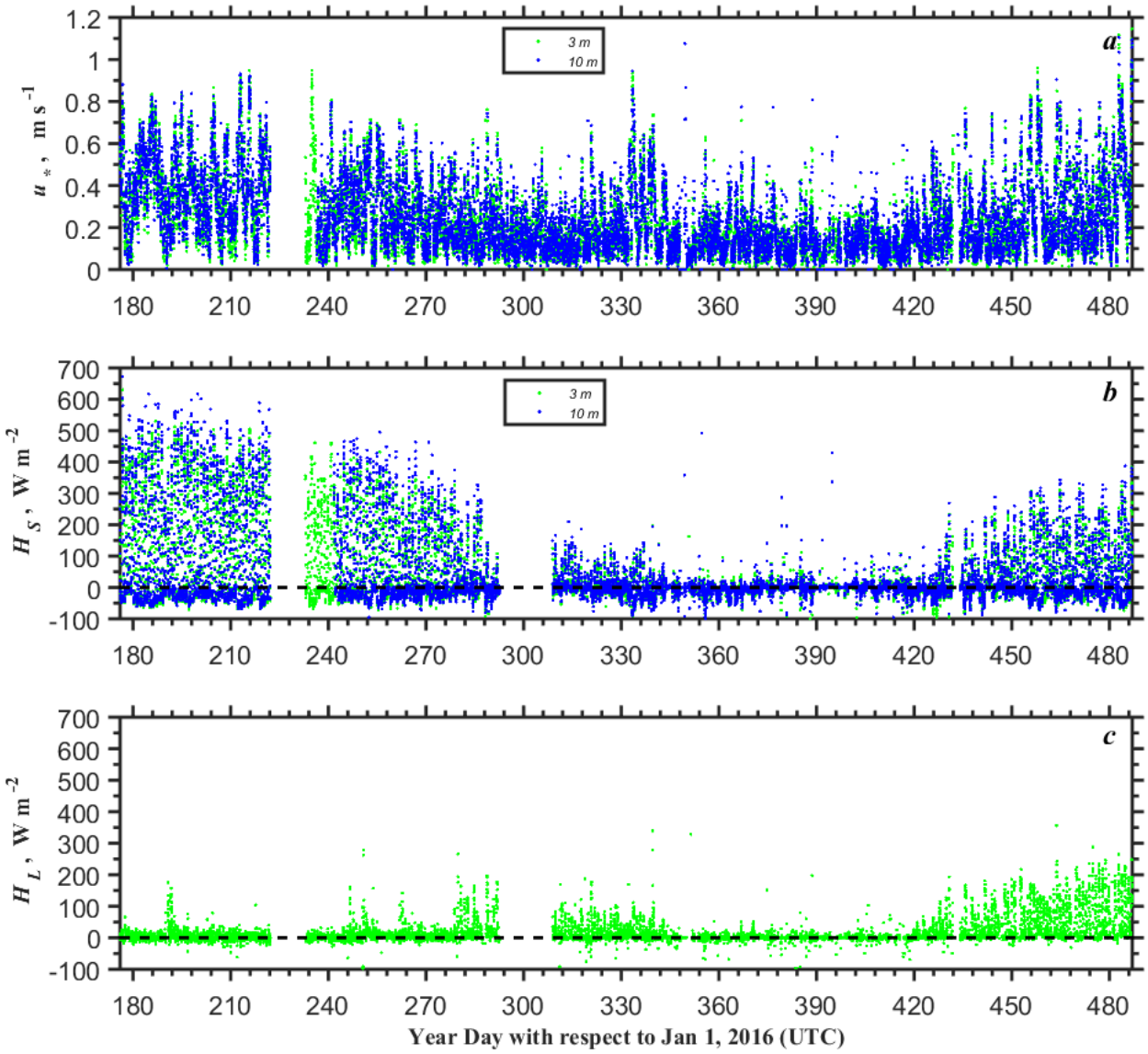

Figure 6. Time series of (*a*) friction velocity observed at 3 and 10 m, (*b*) sensible heat flux observed at 3 and 10 m, and (*c*) latent heat (water vapor) flux for year days 176–487 (24 June 2016-01 May 2017) observed at Columbia River Gorge, OR during WFIP 2 Project. The data are based on half-hour averaging.

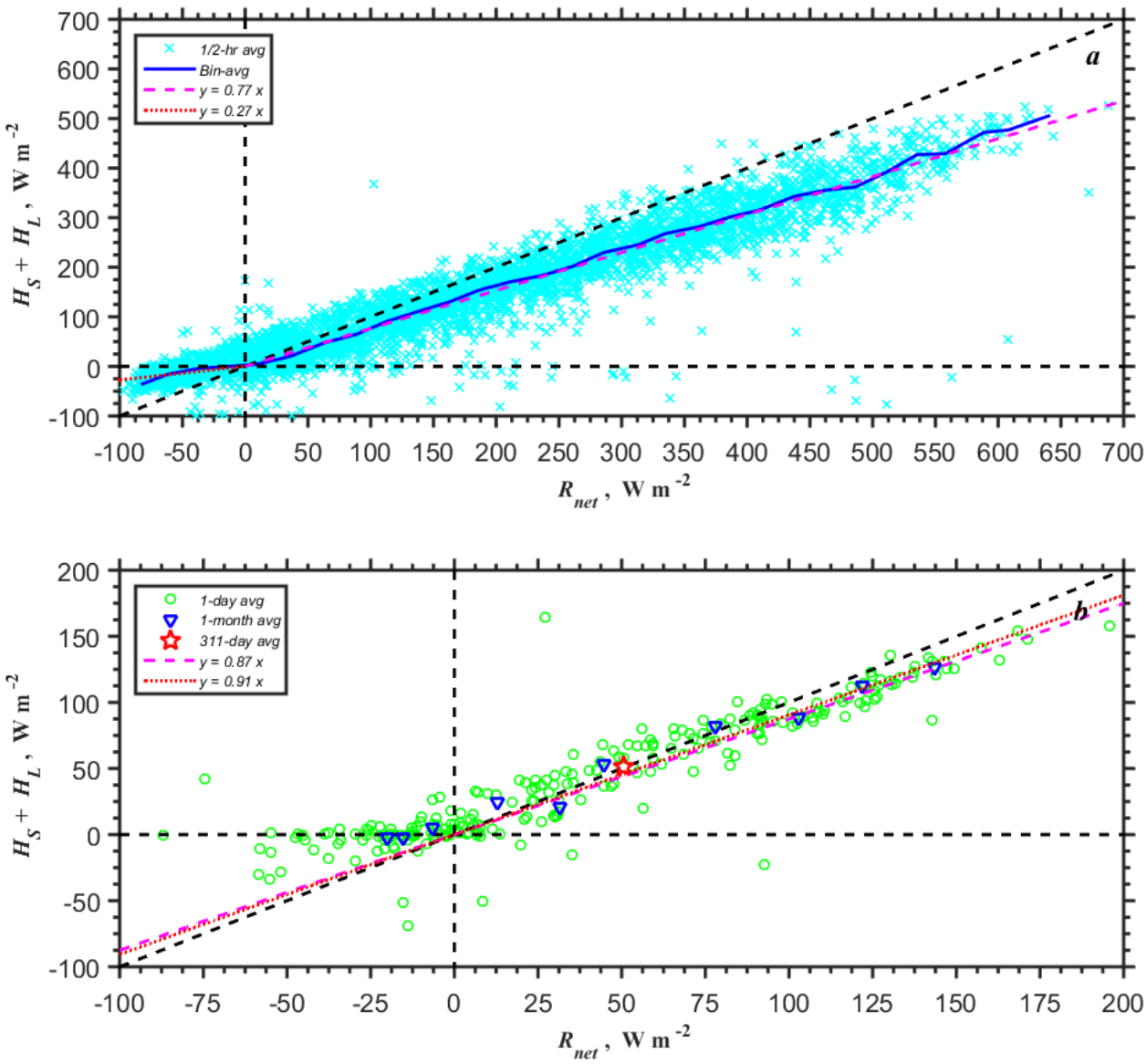

Figure 7. Scatter plots of the sum of the sensible and latent heat fluxes $H_S + H_L$ versus the net solar radiation R_{net} based on (*a*) the half-hourly averaged (symbols) and the bin-averaged (solid line) data and (*b*) the daily, monthly and 311-day (the entire dataset) averaged fluxes for the entire dataset collected at Columbia River Gorge, OR during WFIP 2 Project during year days 176–487 (24 June 2016-01 May 2017).

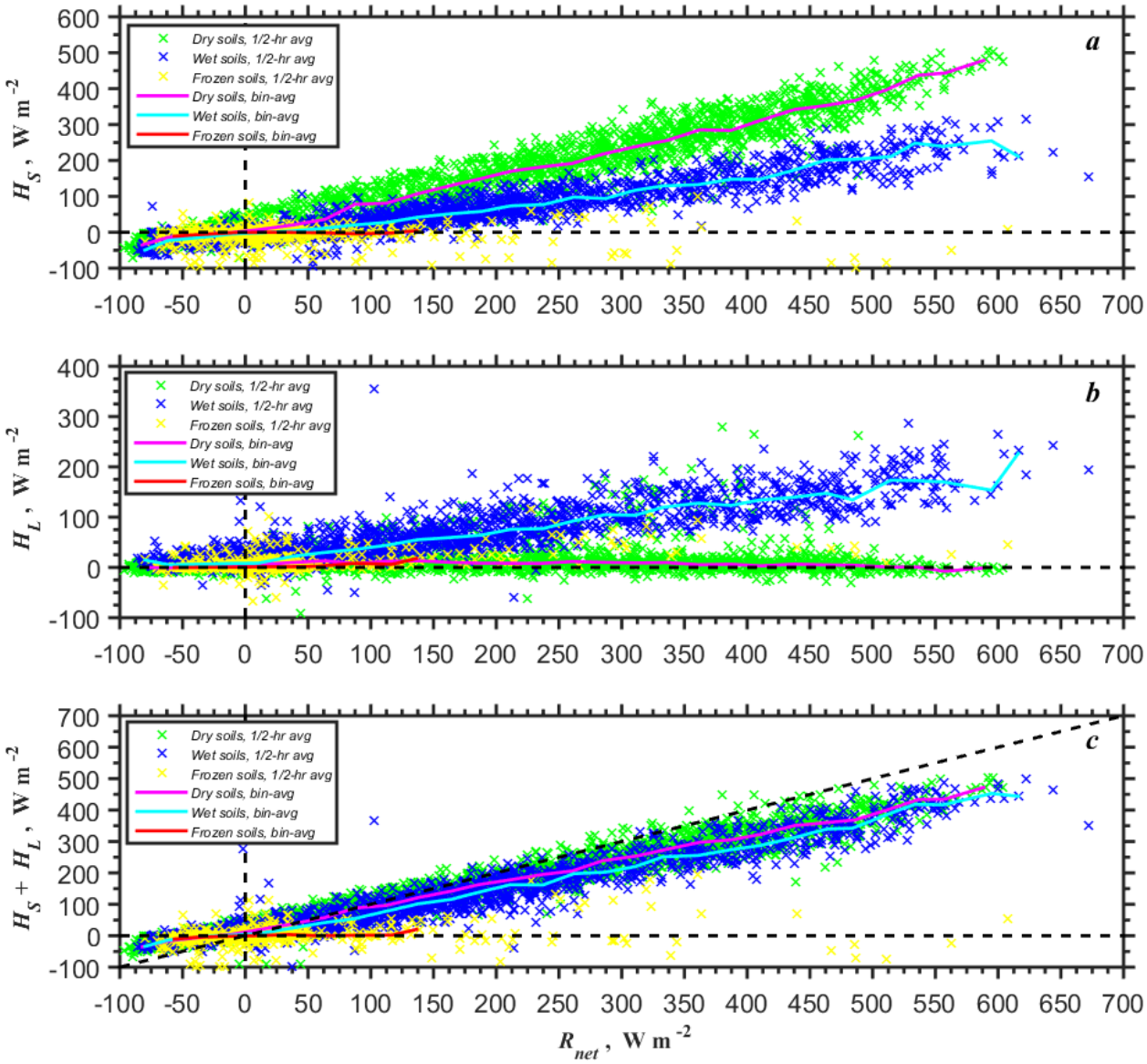

Figure 8. Plots of the bin-averaged (solid lines) and 0.5-hr averaged (symbols) turbulent fluxes (eddy-covariance) of (*a*) sensible heat H_S, (*b*) latent heat H_L, and (c) the sum $H_S + H_L$ (SEB turbulent flux components) versus the net solar radiation R_{net} for dry, wet, and frozen soils observed at Columbia River Gorge, OR during WFIP 2 Project during year days 176–487 (24 June 2016-01 May 2017).

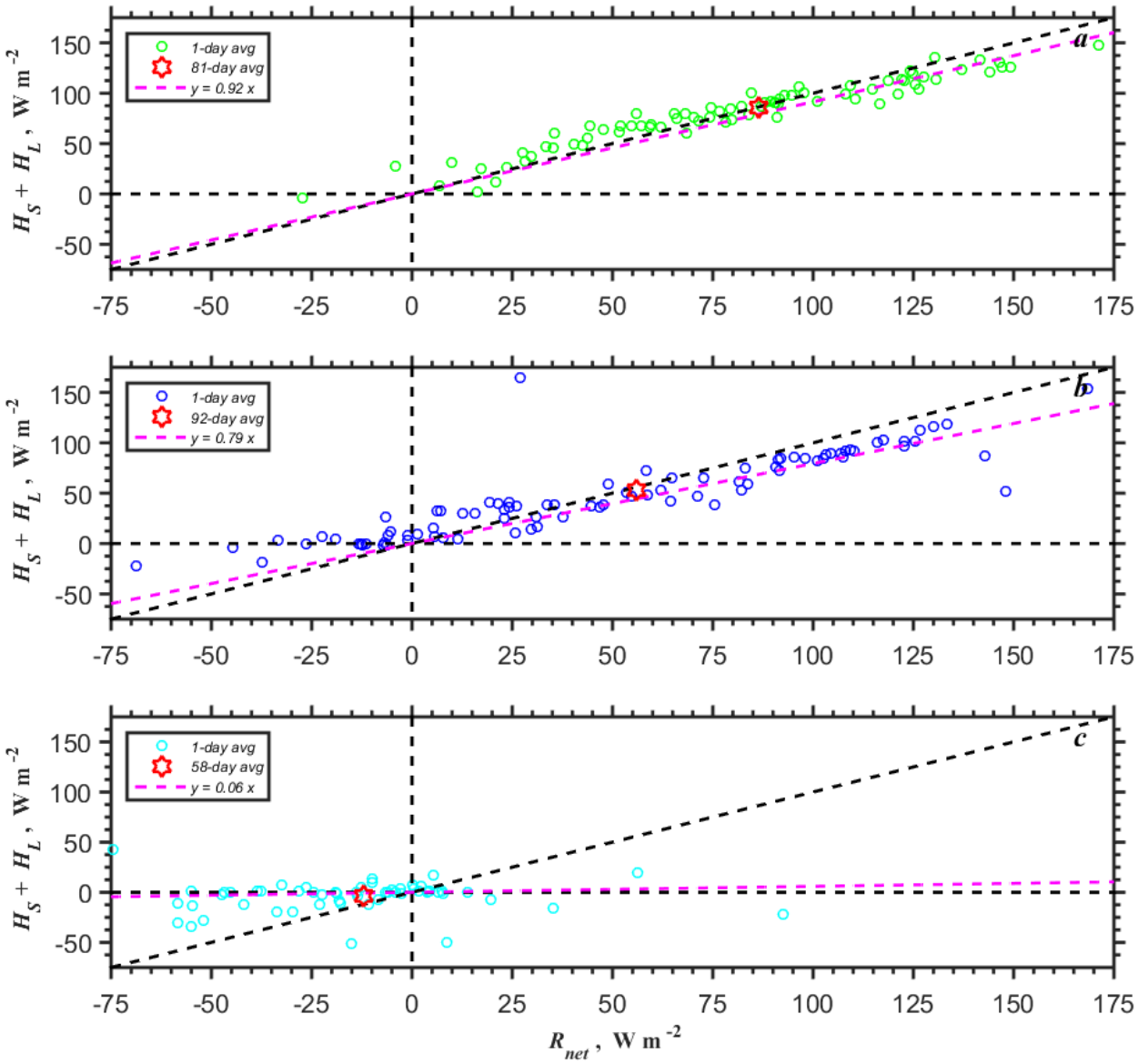

Figure 9. Plots of the sum of the sensible and latent heat fluxes $H_S + H_L$ versus the net solar radiation R_{net} separately for (a) dry, (b) wet, and (c) frozen (snow covered) soils based on daily averaged fluxes and entire dataset averaging (81, 92, and 58-day averaging in each case respectively).

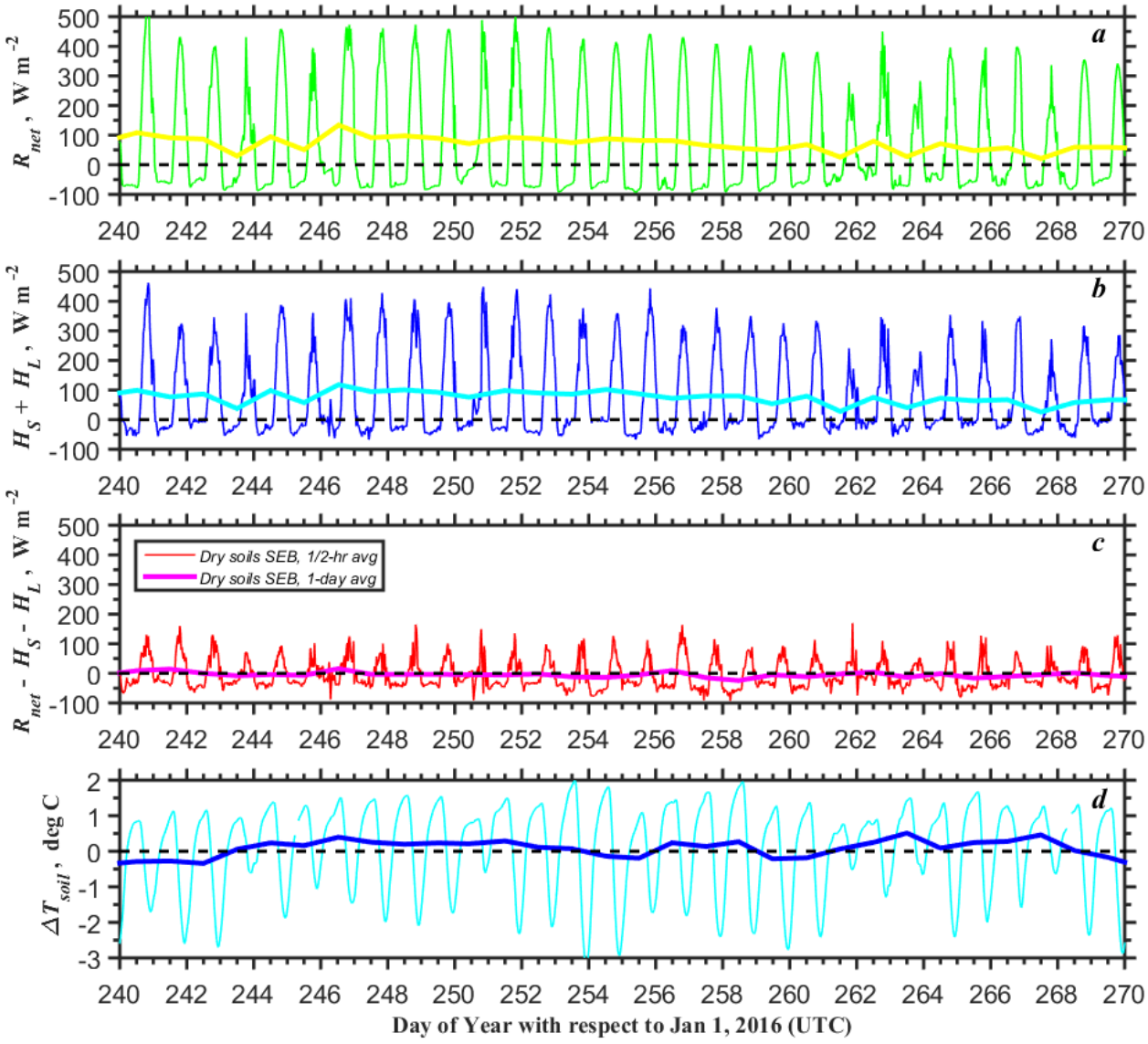

Figure 10. One-month (30-day) time series of (*a*) the net solar radiation R_{net}, (*b*) the sum of the sensible and latent heat fluxes $H_S + H_L$, (*c*) the residual energy $R_{net} - H_S - H_L$ and (*d*) difference of the soil temperature between 10 cm and 5 cm levels for dry soils observed at the WFIP 2 Physics site PS01 during year days 240–270 (27 August-26 September 2016). The data are based on half-hour and daily averaging.

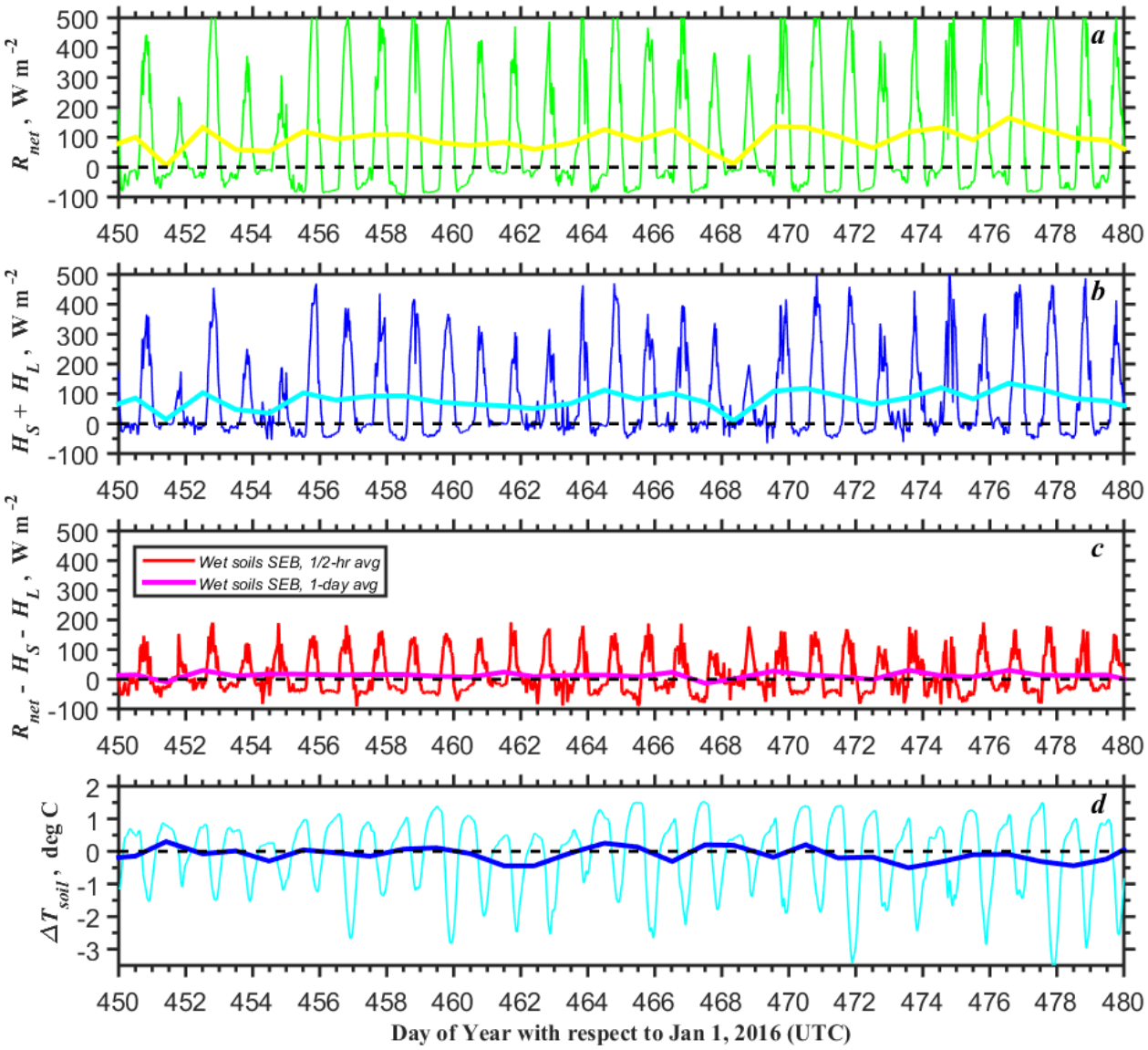

Figure 11. Same as Fig. 10 but for wet soils observed at the WFIP 2 Physics site PS01 during year days 450–480 (25 March-24 April 2017). The data are based on half-hour and daily averaging.

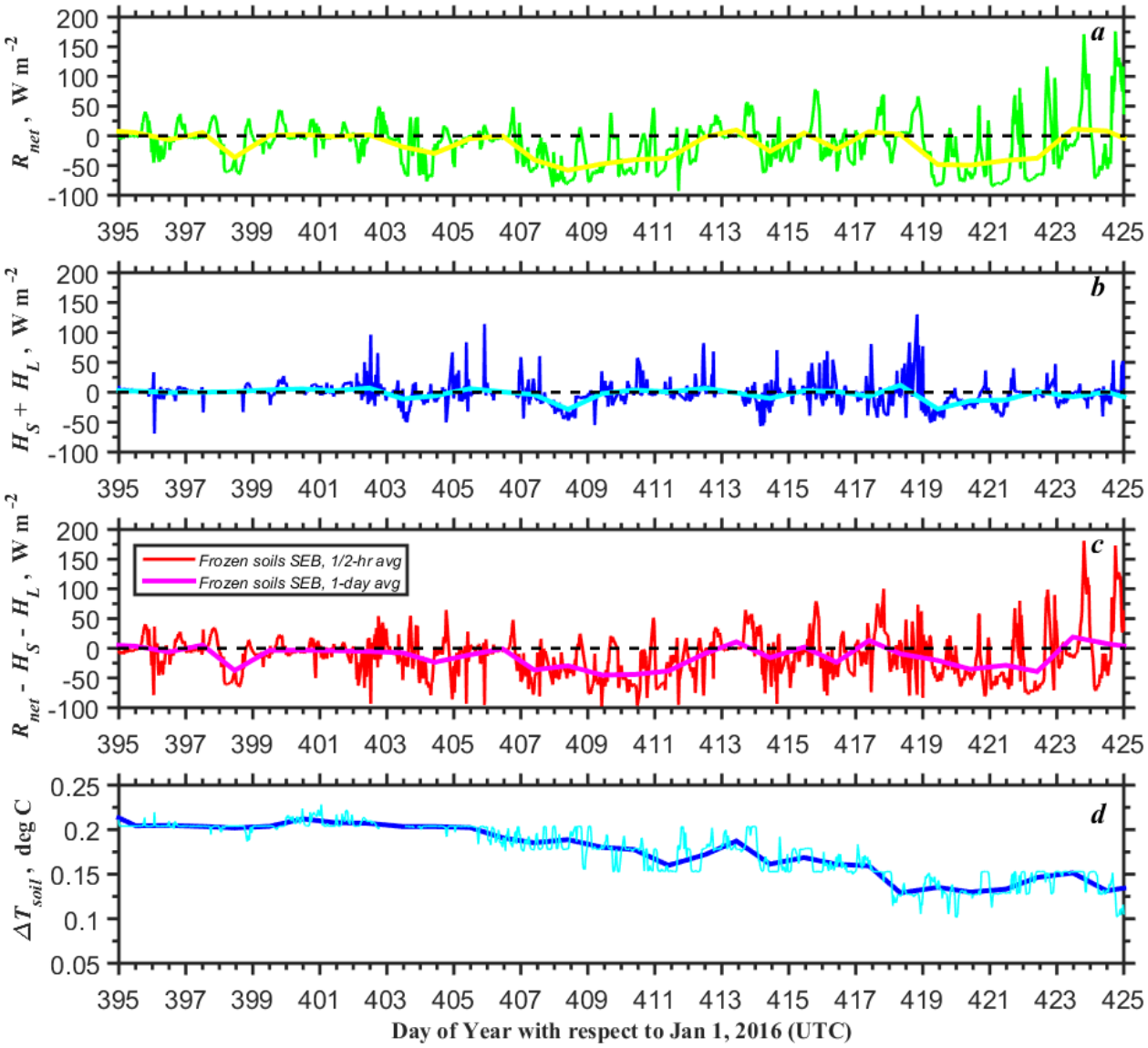

Figure 12. Same as Fig. 10 but for frozen (snow covered) soils observed at the WFIP 2 Physics site PS01 during year days 395–425 (29 January-28 February 2017). The data are based on half-hour and daily averaging.

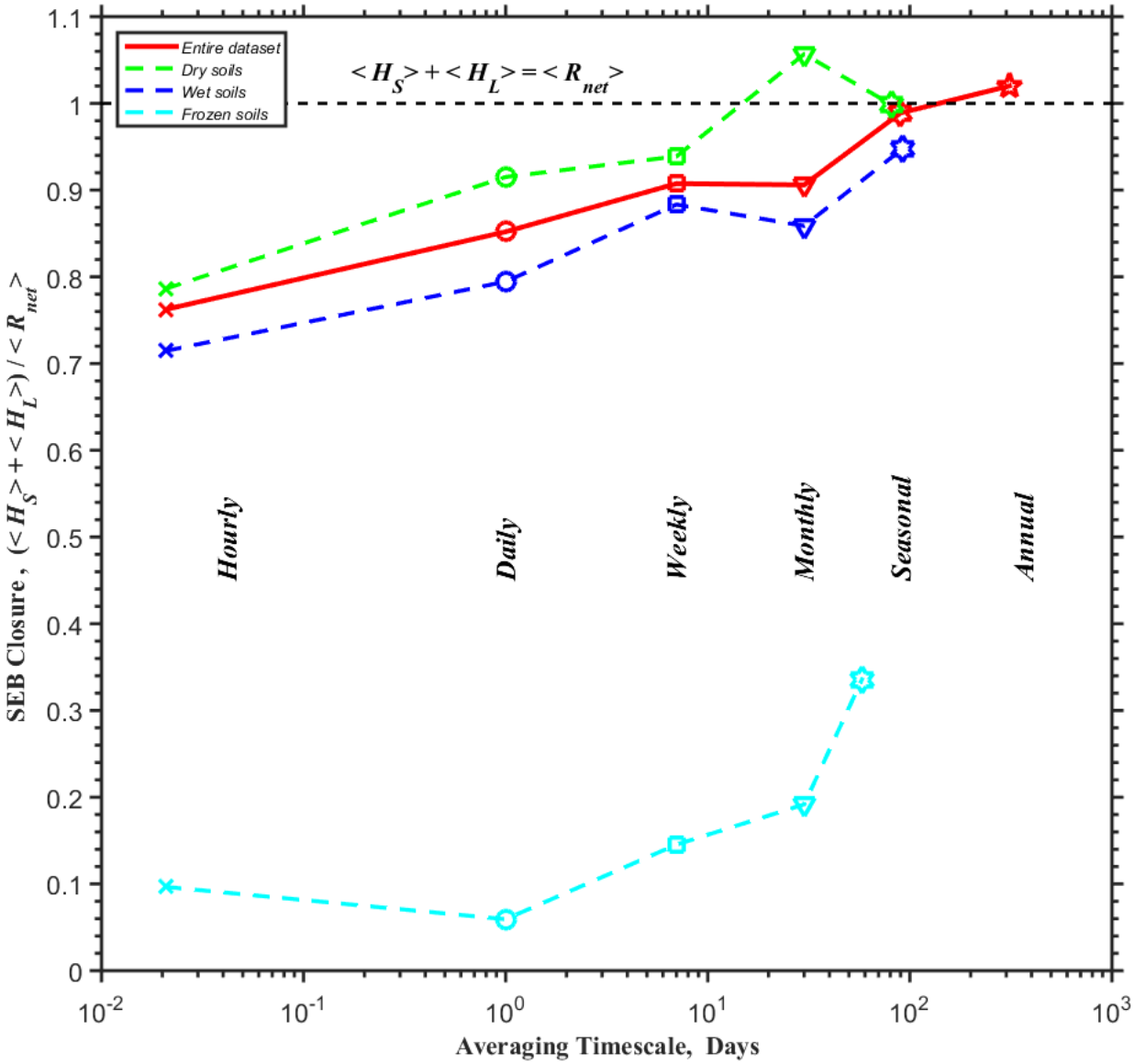

Figure 13. The surface energy balance (SEB) closure at different temporal scales: ratio of turbulent energy fluxes $H_S + H_L$ to net solar radiation R_{net} for the entire dataset (red solid line and red symbols) and separately for different soil types plotted versus averaging time based on the data collected at Columbia River Gorge, OR during WFIP 2 Project.

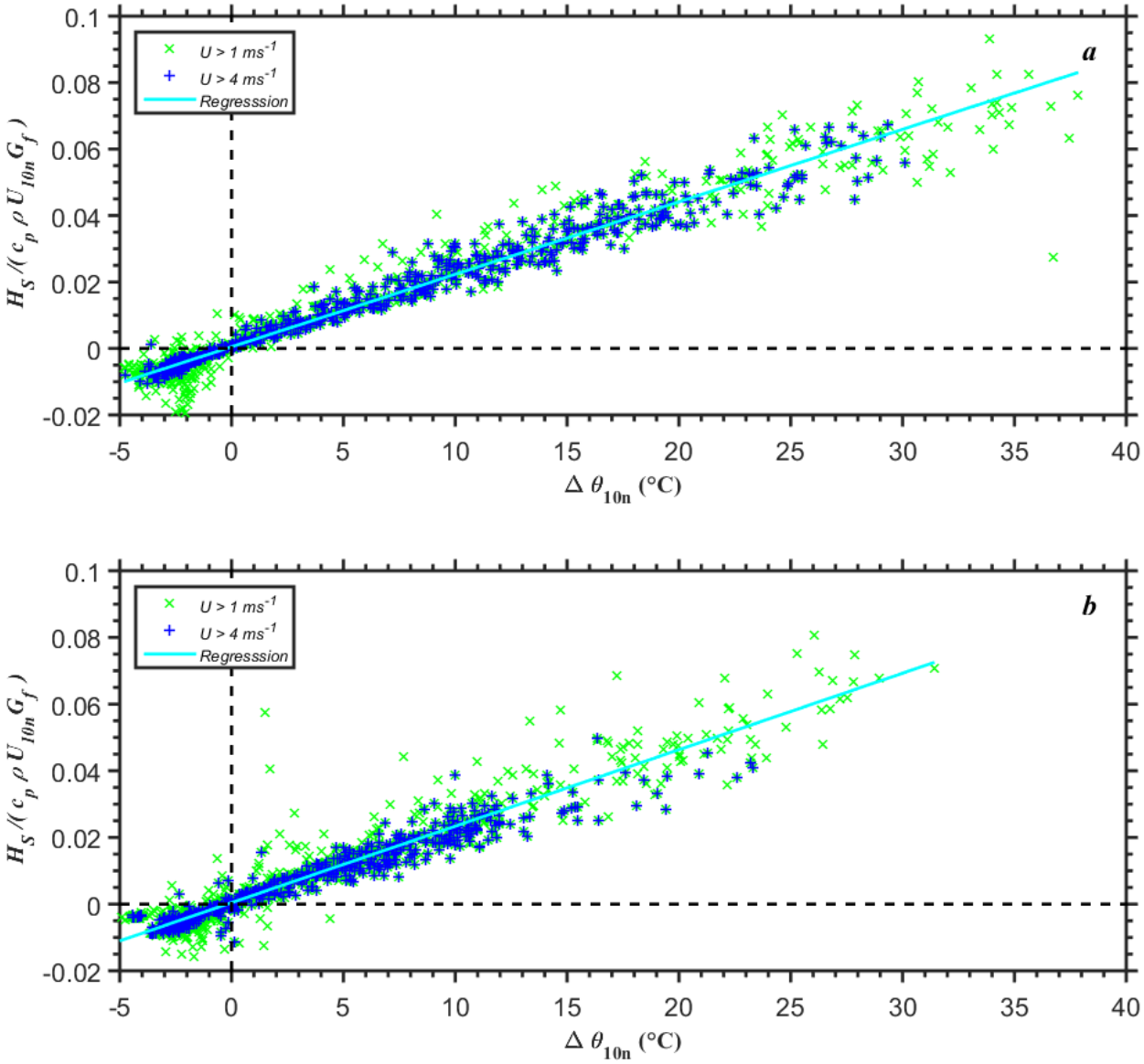

Figure 14. Linear regression fit of normalized half-hourly averaged covariance sensible heat flux versus 10-m neutral surface-air temperature difference for (*a*) the dry soil "golden files" (year days 240–270, 27 August-26 September 2016) and (*b*) the wet soil "golden files" period (year days 450–480, 25 March-24 April 2017). The green ×-symbols are data for 10-m neutral wind speed greater than 1 ms^{-1}; for blue +-symbols only wind speed greater than 4 ms^{-1} are considered.

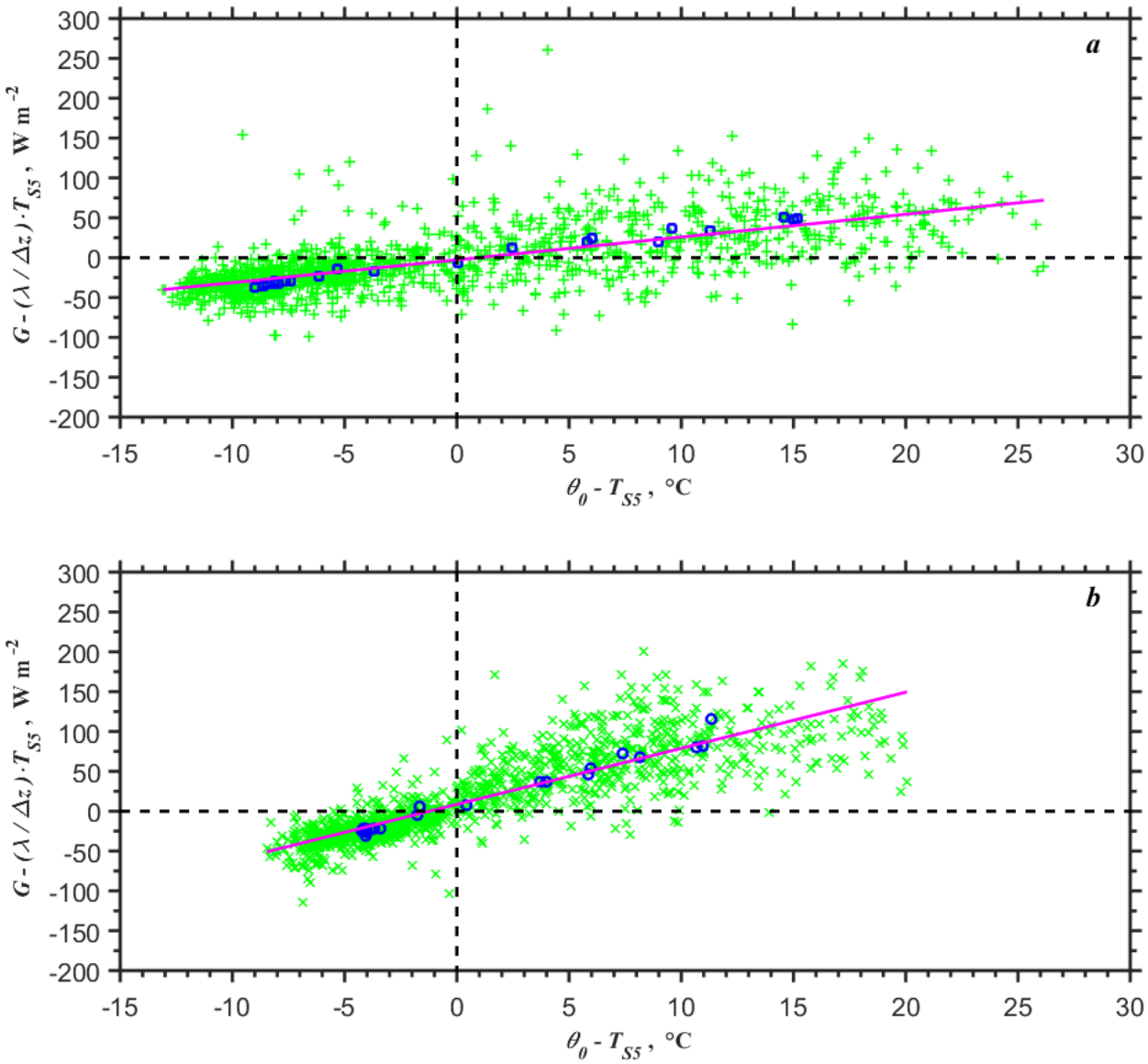

Figure 15. Storage term adjusted ground flux (residual) versus temperature difference between surface (θ_0) and soil at 5 cm depth (T_{S5}) for (*a*) the dry soil "golden files" period (year days 240–270) and (*b*) the wet soil "golden files" period (year days 450–480). The green ×-symbols are half-hourly averaged values; blue circles are derived from the mean diurnal cycle. The magenta solid line is a regression with $\lambda/\Delta z = 2.859 \mathrm{Wm^{-2}K^{-1}}$ for the dry soils and $\lambda/\Delta z = 7.034 \mathrm{Wm^{-2}K^{-1}}$ for the wet soils.

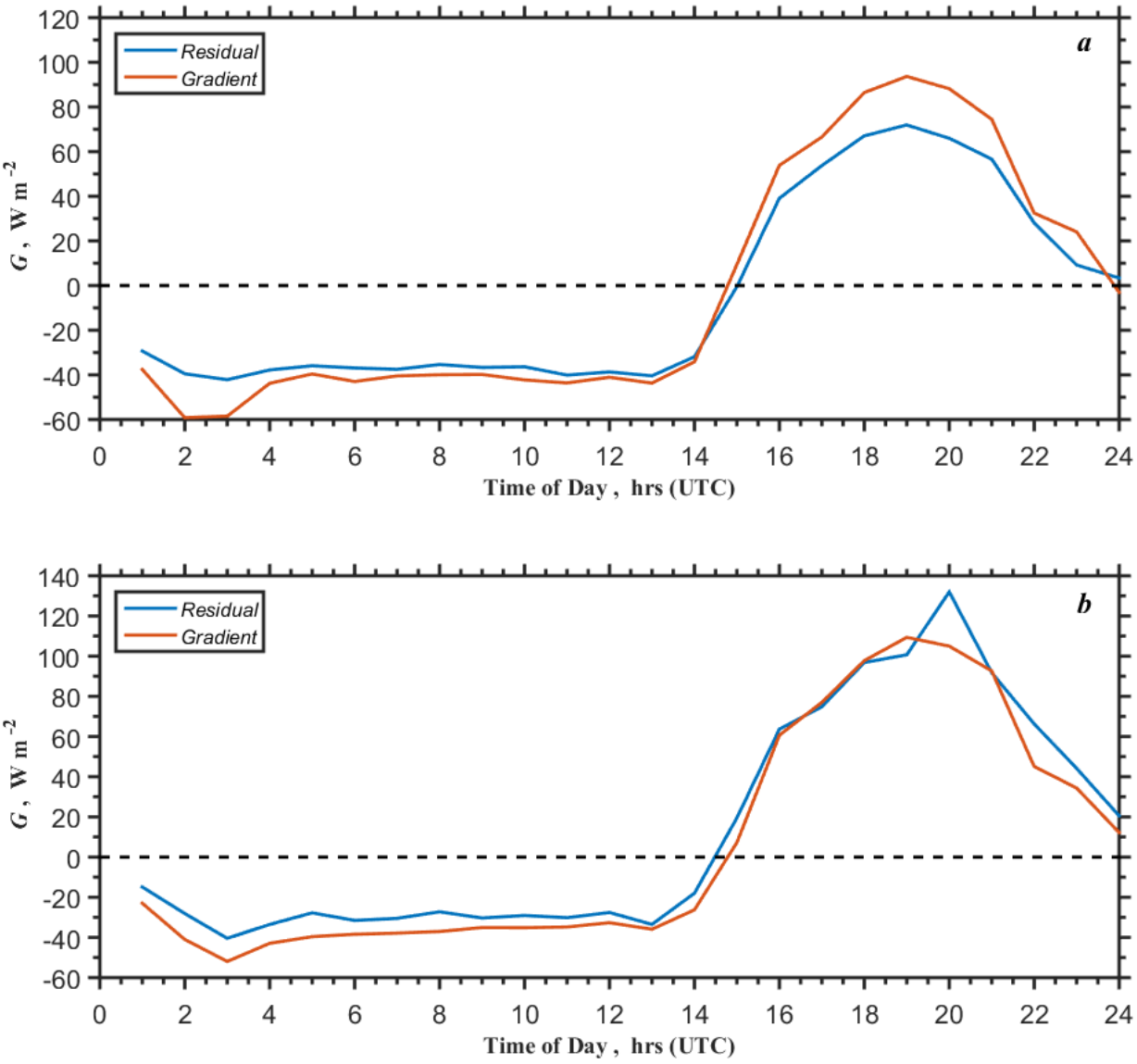

Figure 16. Mean diurnal plot of ground flux G for (a) the dry soil "golden files" period (year days 240–270) and (b) the wet soil "golden files" period (year days 450–480). The blue lines are the residual estimate of G and the red lines are G computed via (20).

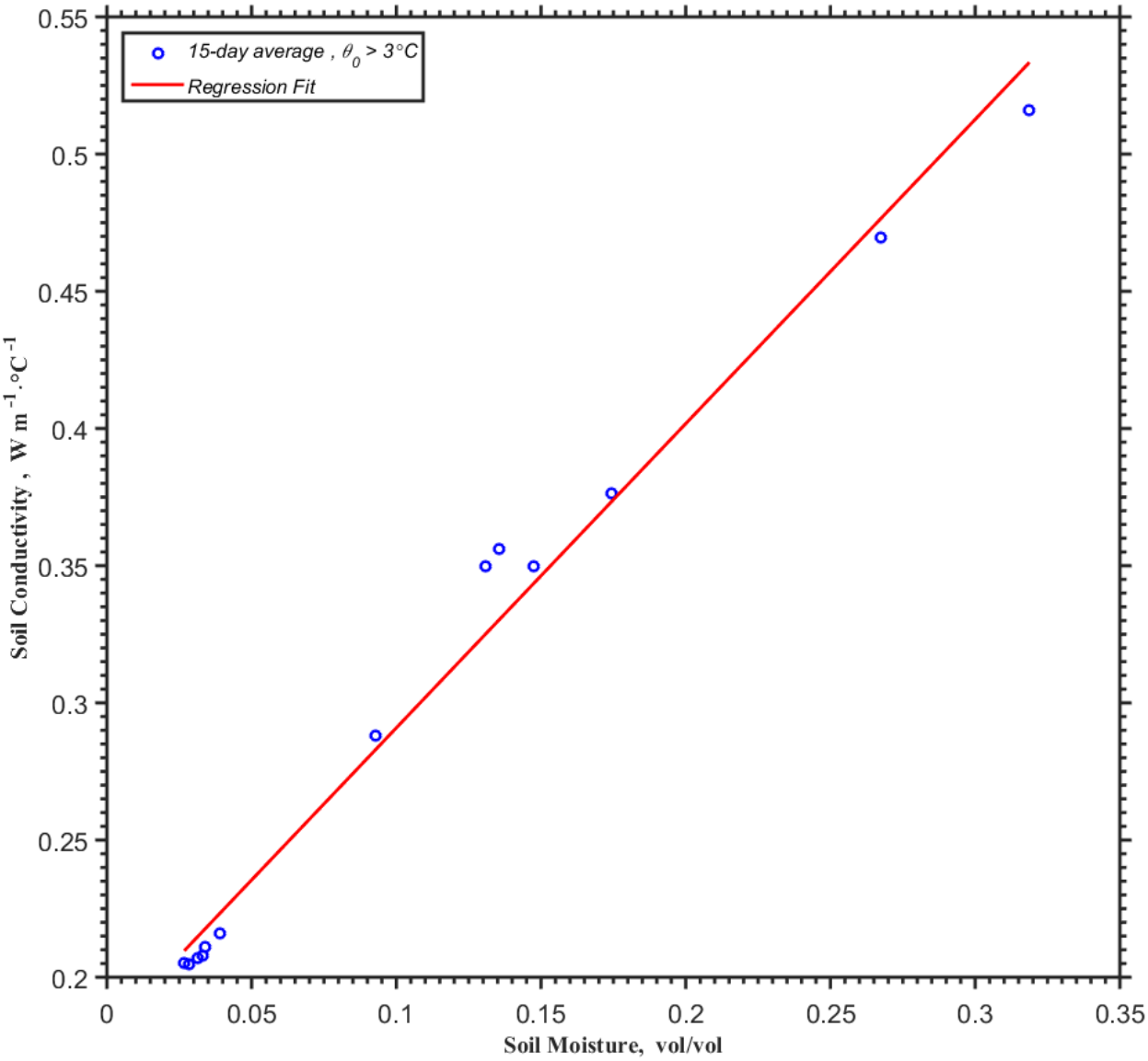

Figure 17. Regression fit of the thermal conductivity of the soil λ versus soil moisture content at 5 cm depth Q_{S5}, see Eq. (25).

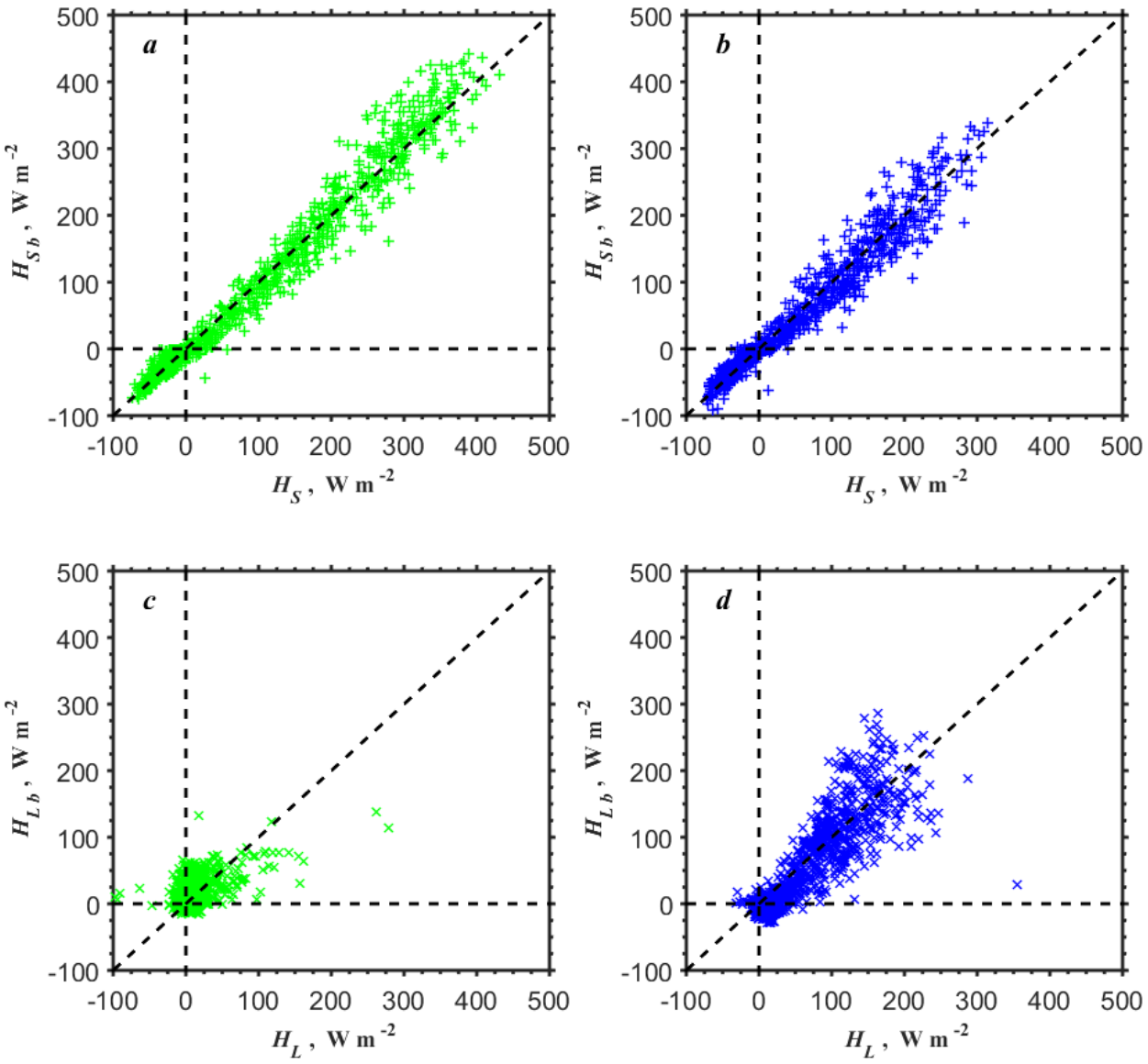

Figure 18. Scatter plots of the bulk estimates of (*a*, *b*) sensible heat flux H_S and (*c*, *d*) latent heat flux H_L versus their measured (direct covariance) counterparts based on the half-hourly averaged data using (16) and (17) with $\phi = 0.4 + 5Q_{S5}$ (ϕ not to exceed 1.45). Plots in the left panels (*a*, *c*) represent the dry soil "golden files" (year days 240–270) and the right panels (*b*, *d*) represent the wet soil "golden files" period (year days 450–480).

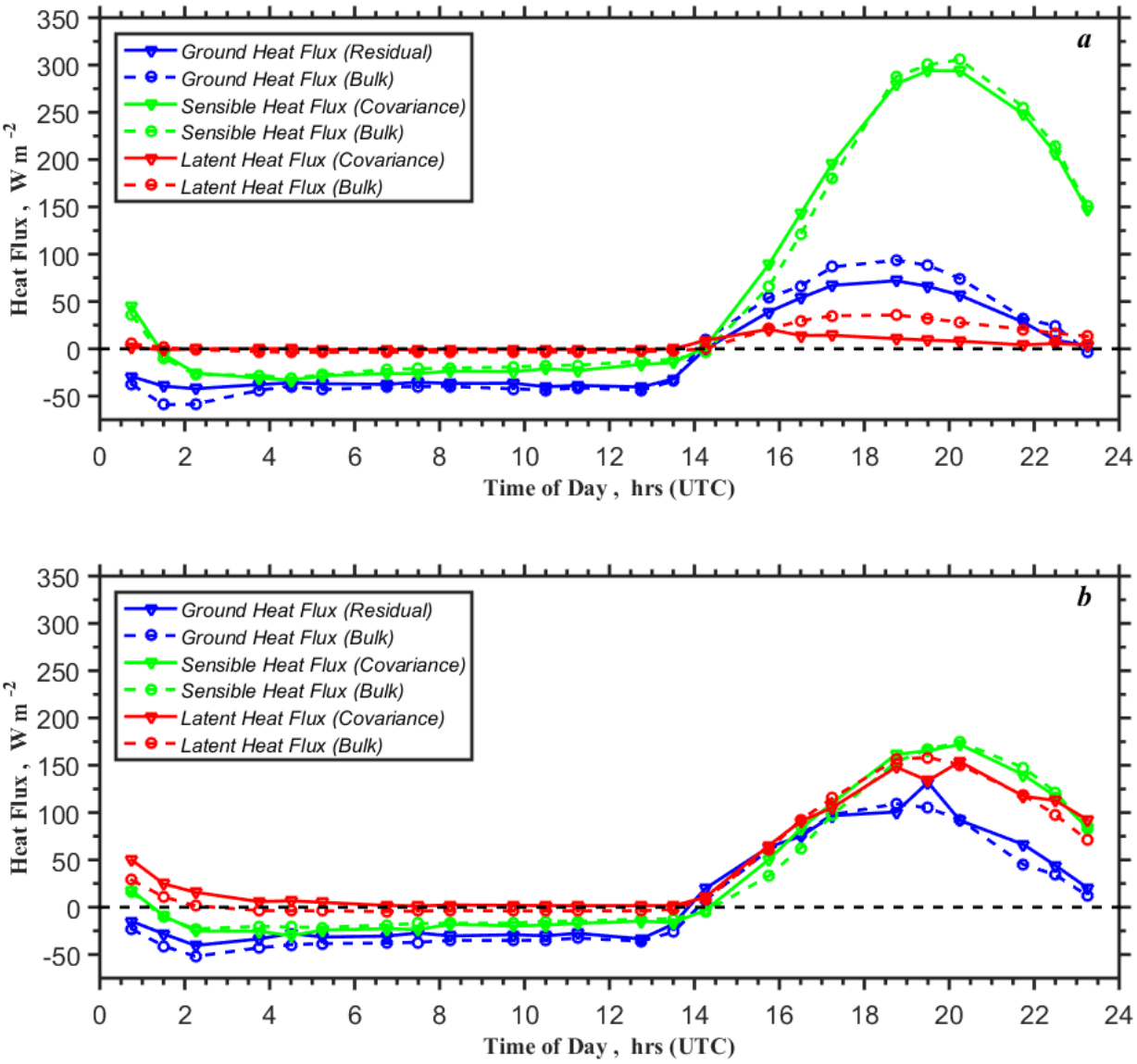

Figure 19. Mean diurnal cycle of sensible, latent, and ground heat fluxes for (*a*) dry and (*b*) wet soil "golden files" periods. Direct measurements are solid lines with triangle symbols; the bulk estimates are dashed lines with circle symbols.

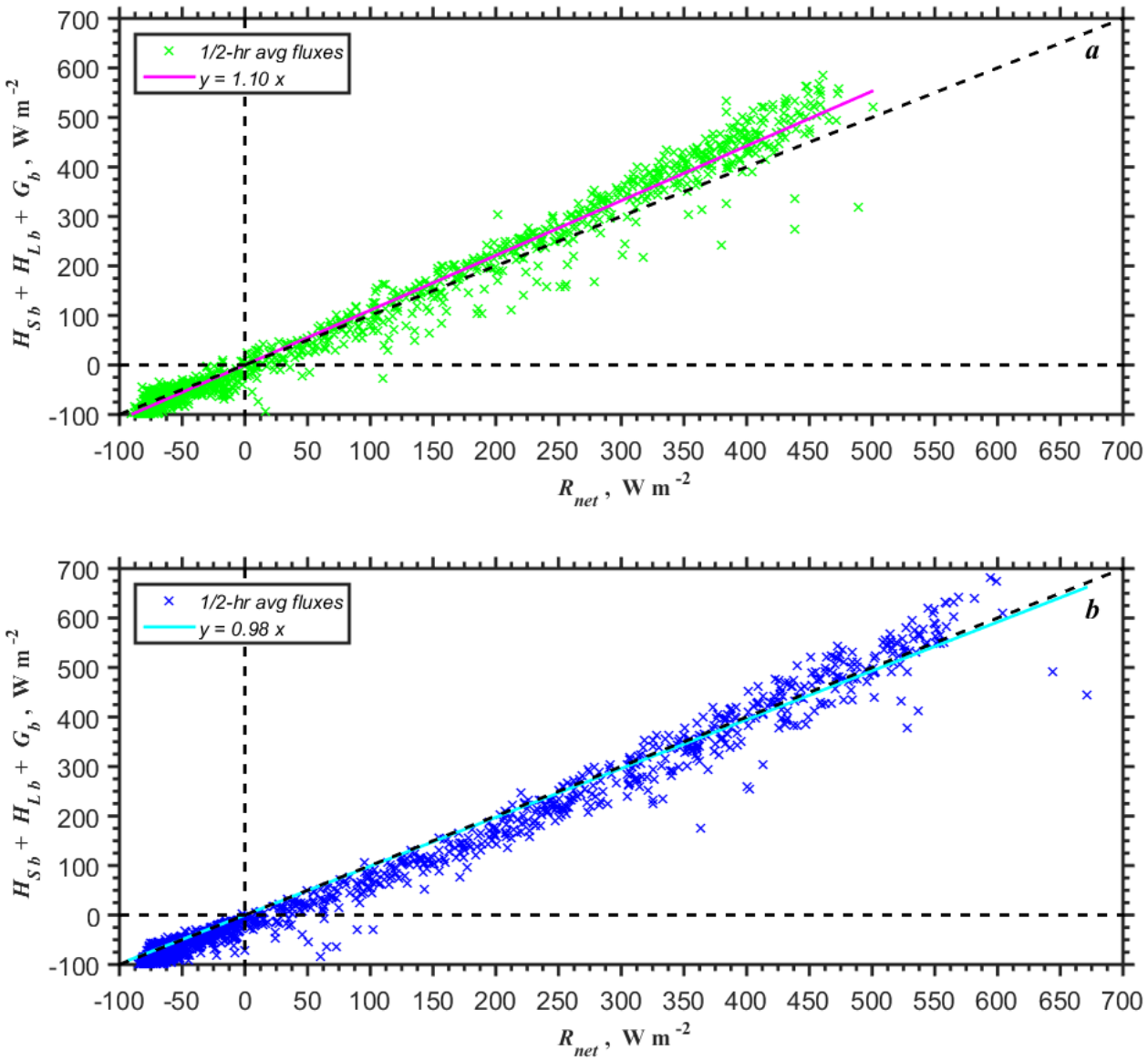

Figure 20. Net surface energy balance from bulk flux calculations for (*a*) the dry soil "golden files" (year days 240–270) and (*b*) the wet soil "golden files" period (year days 450–480). Observed net radiation R_{net} versus the sum of the sensible, latent and ground fluxes as yielded by (10), (16), and (20).

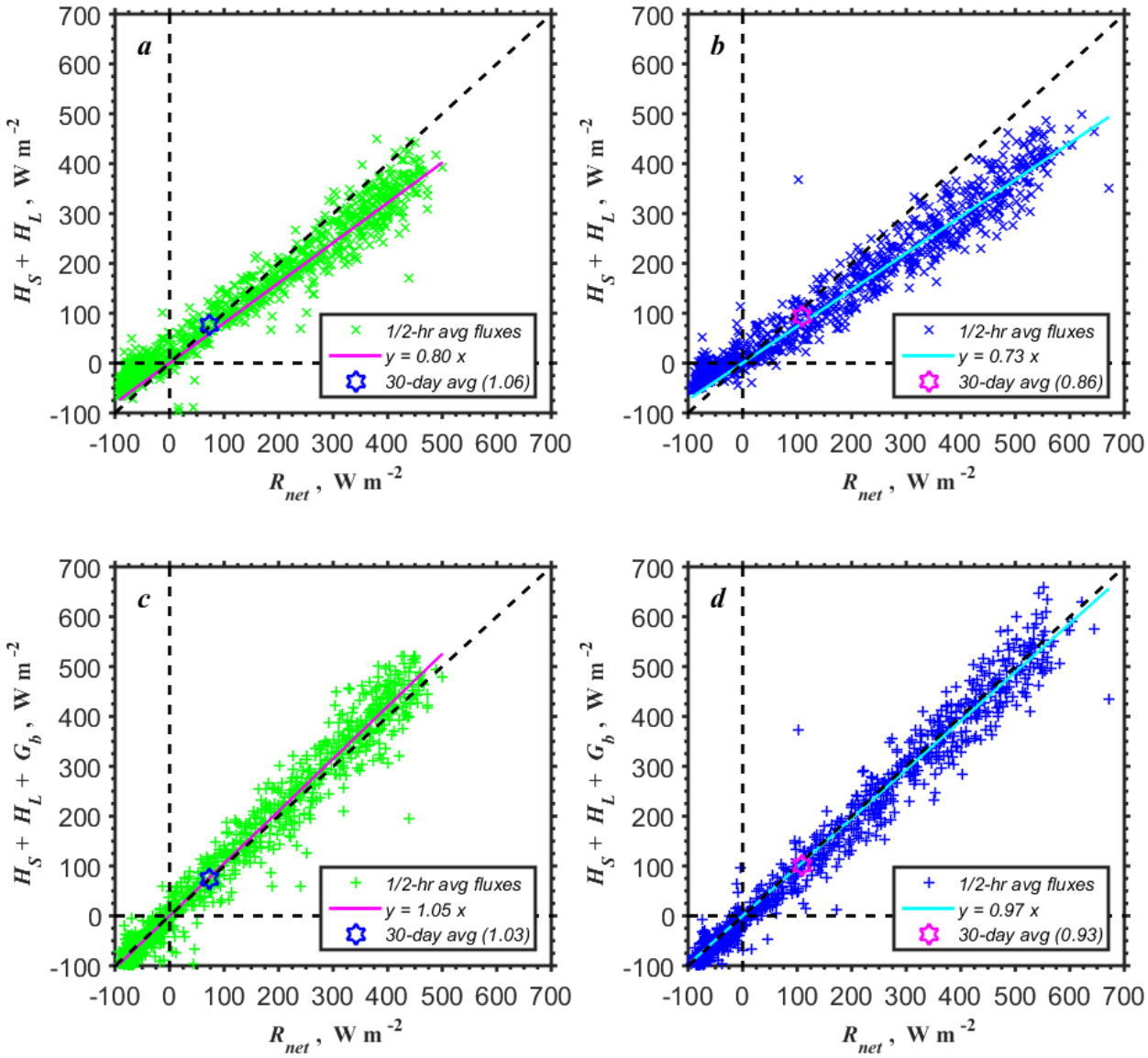

Figure 21. Scatter plots of the net surface energy balance for (*a*, *b*) the sum of the measured sensible and latent heat fluxes $H_S + H_L$ and (*c*, *d*) the sum of the measured $H_S + H_L$ and bulk estimates of the ground heat flux G_b versus the net solar radiation R_{net} based on the half-hourly and monthly averaged data. Plots in the left panels (*a*, *c*) represent the dry soil "golden files" (year days 240–270) and the right panels (*b*, *d*) represent the wet soil "golden files" period (year days 450–480).